

Benchmarking Immersed Boundary Models of Viscoelastic Flows Through Complex Geometries

Cole Gruninger¹, Aaron Barrett², Fuhui Fang¹, M. Gregory Forest^{1,3–5}, and Boyce E. Griffith^{1,3–7,*}

¹Department of Mathematics, University North Carolina, Chapel Hill, NC, USA

²Department of Mathematics, University of Utah, Salt Lake City, UT, USA

³Department of Applied Physical Sciences, University of North Carolina, Chapel Hill, NC, USA

⁴Department of Biomedical Engineering, University of North Carolina, Chapel Hill, NC, USA

⁵Carolina Center for Interdisciplinary Applied Mathematics, University of North Carolina, Chapel Hill, NC, USA

⁶Computational Medicine Program, University of North Carolina School of Medicine, Chapel Hill, NC, USA

⁷McAllister Heart Institute, University of North Carolina School of Medicine, Chapel Hill, NC, USA

*To whom correspondence should be addressed; email: boyceg@email.unc.edu

September 8, 2023

Abstract

We present and analyze a series of benchmark tests regarding the application of the immersed boundary (IB) method to viscoelastic flows through and around non-trivial, stationary geometries. The IB method is widely used for the simulation of biological fluid dynamics and other problems where a structure is immersed in a fluid. Although the IB method has been most commonly used to model systems with viscous incompressible fluids, it also can be applied to viscoelastic fluids, and has enabled the study of a wide variety of dynamical problems including the settling of vesicles and the swimming of fibers in Oldroyd-B fluids. However, to date, relatively little work has explored the accuracy or convergence properties of the numerical scheme. Herein, we present benchmarking results for an IB solver applied to viscoelastic flows in and around non-trivial geometries using the idealized Oldroyd-B and molecularly-based Rolie-Poly constitutive equations. We consider a variety of test cases, some inspired from experimental flow geometries and others based on numerical benchmarks obtained from more traditional finite element and finite volume methods. The IB method is compared against more complex finite element and finite volume viscoelastic flow solvers and, where possible, to rheology experiments. Additionally, we analyze different choices of regularized delta function and relative Lagrangian grid spacings which allow us to identify and recommend the key choices of these numerical parameters depending on the present flow regime.

1 Introduction

The immersed boundary (IB) method is a mathematical formulation and numerical scheme utilized to model the presence of a structure immersed in a fluid.^{1,2} The IB method was originally developed by Peskin to model the flow of blood within the heart.^{3,4} The IB method has since been adapted to study a variety of fluid-structure interaction (FSI) problems spanning applications from a broad array of fields, including cardiac mechanics,^{5–9} platelet adhesion and aggregation,^{10,11} insect flight,^{12,13} and undulatory swimming.^{14–19} The IB method employs a combination of Lagrangian and Eulerian variables that interact with one another through the action of integral transforms with the Dirac delta function. In the IB formulation, the velocity and incompressibility of the fluid-structure system are described using Eulerian variables, and the configurations of the immersed structures and their resultant forces are described using Lagrangian variables. The Eulerian variables are discretized on a structured Cartesian grid and the Lagrangian variables are discretized on a curvilinear mesh that moves freely through the Cartesian grid without needing to conform to it. Interactions between the Eulerian and Lagrangian variables is mediated through discretized

integral transforms against a regularized Dirac delta kernel function which are used both to interpolate the discrete Eulerian velocity onto the Lagrangian curvilinear mesh and also to spread forces from the Lagrangian curvilinear mesh onto the Cartesian grid.

The IB method was introduced and is still typically employed using a Newtonian description of the fluid, in which the stress tensor associated with the fluid is linearly related to the fluid's velocity gradient. Fluids that are comprised of small, relatively inert molecules can be accurately modeled using a Newtonian description; examples are water, liquid nitrogen, and liquid argon. The success of the Newtonian description hinges on the assumption that, even for turbulent flows, intermolecular distances between the neighboring molecules which make up the fluid are relatively preserved, so that the energy dissipation mechanism, modeled by viscosity in a Newtonian fluid, is constant.²⁰ However, for fluids whose molecular constituents are perturbed by the flow, the energy dissipation mechanism becomes a function of the local flow dynamics and the Newtonian model subsequently breaks down. Fluids for which the Newtonian model fails to provide an adequate description are typically called "complex" or "non-Newtonian" fluids. Non-Newtonian fluids are typically comprised of large polymeric molecules (chains) that, either individually at dilute concentrations, or at the scale of entanglements at higher concentrations, can be stretched out of their equilibrium configurations leading to modes of storage and relaxation of stresses in response to gradients present in the velocity field. Consequently, many non-Newtonian fluids display simultaneously the behaviours of a viscous liquid and an elastic solid. Such fluids are appropriately termed "viscoelastic" fluids. Eulerian models of viscoelasticity, such as the Oldroyd-B model,²¹ incorporate a separate evolution equation for the stress which is typically modeled using the frame-invariant upper-convected time derivative, defined by

$$\overset{\nabla}{\mathbb{T}} = \frac{\partial \mathbb{T}}{\partial t} + \mathbf{u} \cdot \nabla \mathbb{T} - \nabla \mathbf{u} \mathbb{T} - \mathbb{T} \nabla \mathbf{u}^T, \quad (1)$$

in which we employ the convention $\nabla \mathbf{u}_{i,j} = \frac{\partial u_i}{\partial x_j}$.

Because the IB method uses regularized delta functions, the IB method is generally only first-order accurate as noted by several prior studies.^{22–26} The intuitive explanation as to why the IB method is generally first-order accurate is that the continuous fluid pressure and normal derivative of the fluid velocity have jump discontinuities across the immersed structure which are smoothed out by the regularized delta function. As a result, fluid stresses generally do not converge pointwise up to the immersed boundary using the IB method. The implication for viscoelastic FSI simulated using the IB method is that the stress, whose evolution depends on the velocity gradient, also should not be expected to converge pointwise up to the interface. Although fluid stresses may not converge pointwise at the interface, in practice, it is observed that the velocity does converge pointwise at a first-order rate. This finding was first proved for the case of an incompressible Newtonian fluid by Mori in the context of Stokes flow.²⁶ Mori also provided a heuristic analysis that concluded that, so long as one refines the Lagrangian mesh spacing proportional to the Eulerian mesh spacing, one should expect the velocity to converge at a second-order rate in the L^1 grid norm, a three-halves rate in the L^2 norm, and a first-order rate in the L^∞ norm. This same L^2 error estimate was proven more recently by Heltai and Lei in the context of a finite element immersed boundary method applied to a simple elliptic equation, for which a priori estimates are readily accessible.²⁷ Subsequent theoretical and empirical work in the context of Stokes flow by Liu and Mori have further analyzed how the accuracy of the velocity is affected by the choice of the regularized delta function employed.²⁸ Liu and Mori's error estimates demonstrated that smoother regularized delta functions are able to remove presence of spurious oscillations or Gibbs type phenomena present in the computed solution. In support of Liu and Mori's finding, Yang et al.²⁹ introduced smoothed versions of some of the regularized delta functions derived by Peskin,^{1,30} and demonstrated empirically that they were better at removing spurious oscillations present in the Lagrangian forces defined along the immersed boundary. More recently, in the context of the immersed finite element/difference (IFED) method, Lee and Griffith³¹ analyzed how the choice of regularized delta function and relative mesh spacing of the Lagrangian and Eulerian grid affects the accuracy of computed Newtonian flows. Lee and Griffith concluded that, so long as pressure loads on the immersed structure are not substantial, using regularized delta functions with narrower supports coupled with a relatively coarse discretization of the Lagrangian structure with respect to the background Eulerian grid provides a substantial increase in accuracy of the IFED method.

Although the IB method has been mostly used in conjunction with Newtonian fluid models, there has been some

previous work with viscoelastic fluid models.^{32–36} These models are based on the Maxwell model, in which an additional viscoelastic stress tensor is evolved with the fluid.²⁰ Despite the recent increase in interest in using the IB method with non-Newtonian fluids, it remains unclear whether the IB method can reliably simulate viscoelastic FSI problems because the polymeric stress tensor evolution directly depends on the velocity gradient. Recall that the velocity gradient cannot be captured pointwise near an immersed boundary, and so the viscoelastic stress, whose evolution depends on the velocity gradient, cannot be expected to converge pointwise near immersed boundaries either. Nonetheless, prior work using the IB method to simulate viscoelastic FSI has demonstrated reasonable results. For instance, Ma et al.³⁷ developed an immersed boundary method with a lattice-Boltzmann fluid solver and were able to achieve convergent velocities, even at high Weissenberg numbers. Stein et al.^{38,39} investigated the IB method in the context of Oldroyd-B fluid models and demonstrated that the viscoelastic stress failed to converge pointwise at the interface. Further, they observed that even though they could obtain convergent net forces on the structure, the forces were inaccurate for under-resolved grids.

Herein, we extend the investigations by Stein et al. further and demonstrate that the IB method used in conjunction with a viscoelastic fluid model obtains pointwise first-order accurate fluid velocities, first and half-order rates of convergence of the viscoelastic stress in the L^1 and L^2 grid norms respectively, and effectively replicates macrorheology experiments. Furthermore, we find that although stresses do not converge pointwise up the immersed boundary, net forces can be computed with first order accuracy by summing over the Lagrangian forces and that the accuracy of computed net forces depend substantially on the regularized delta function and the relative Lagrangian grid spacings employed. This finding is compared against the effect the identity of the regularized delta function and relative Lagrangian grid spacings have on the computed fluid velocity and viscoelastic stresses whose relative accuracies appear to depend on the identity of the regularized delta function, but not the relative Lagrangian grid spacings unless pressure loads on the immersed structure are significant.

2 Model Description

We consider an infinitesimally thin interface $\mathbf{X} \in \Gamma_0$ immersed in an incompressible fluid in a domain $\mathbf{x} \in \Omega$. The fluid is described by a Cauchy stress tensor $\sigma(\mathbf{x}, t)$ and velocity $\mathbf{u}(\mathbf{x}, t)$. The configuration of the interface at time t is given by the mapping $\chi(\mathbf{X}, t) \in \Gamma_t$. The equations of motion are

$$\rho \left(\frac{\partial \mathbf{u}(\mathbf{x}, t)}{\partial t} + \mathbf{u}(\mathbf{x}, t) \cdot \nabla \mathbf{u}(\mathbf{x}, t) \right) = \nabla \cdot \sigma(\mathbf{x}, t) + \mathbf{f}(\mathbf{x}, t), \quad (2)$$

$$\nabla \cdot \mathbf{u}(\mathbf{x}, t) = 0, \quad (3)$$

$$\mathbf{f}(\mathbf{x}, t) = \int_{\Gamma_0} \mathbf{F}(\mathbf{X}, t) \delta(\mathbf{x} - \chi(\mathbf{X}, t)) dA, \quad (4)$$

$$\frac{\partial \chi(\mathbf{X}, t)}{\partial t} = \mathbf{U}(\mathbf{X}, t) = \int_{\Omega} \mathbf{u}(\mathbf{x}, t) \delta(\mathbf{x} - \chi(\mathbf{X}, t)) d\mathbf{x}, \quad (5)$$

in which ρ is the density of the fluid, $\mathbf{f}(\mathbf{x}, t)$ is the Eulerian body force density, $\mathbf{F}(\mathbf{X}, t)$ is the Lagrangian force density, and $\mathbf{U}(\mathbf{X}, t)$ is the Lagrangian velocity. Equations (2) and (3) describe the conservation of momentum and the incompressibility constraint on the velocity field, respectively. Equation (5) specifies that the immersed boundary moves according to the local fluid velocity. The Lagrangian force density $\mathbf{F}(\mathbf{X}, t)$ generated as a result of that movement induces an Eulerian force density $\mathbf{f}(\mathbf{x}, t)$ through equation (4). The integral transforms against the Dirac delta function present in equations (4) and (5) are the heart of the mathematical formulation of the IB method and establish the FSI coupling between the immersed boundary and the fluid. In this study, we focus on the case in which the position of the immersed boundary is fixed for which the interface force density $\mathbf{F}(\mathbf{X}, t)$ is a Lagrange multiplier enforcing the rigidity of the interface. Although it is possible to devise IB methods that determine the exact Lagrange multiplier force density $\mathbf{F}(\mathbf{X}, t)$,^{40,41} we instead approximate the Lagrange multiplier force density by a penalty spring force which opposes the motion of the immersed boundary

$$\mathbf{F}(\mathbf{X}, t) = \kappa(\chi(\mathbf{X}, 0) - \chi(\mathbf{X}, t)), \quad (6)$$

in which κ is the stiffness parameter. We choose to use this penalty force formulation in order to avoid solving the poorly conditioned extended saddle-point system imposed by using an exact Lagrange multiplier formulation. In practice, we choose the stiffness parameter κ to be the largest stable value permitted by the numerical scheme so the Lagrangian markers used to discretize the structure move a distance no more than $\frac{h}{2}$, in which h is the finest Cartesian meshwidth used in a particular simulation.

The viscoelastic fluid models considered in this paper are ones in which the total stress $\sigma(\mathbf{x}, t)$ can be decomposed into a Newtonian solvent and polymeric stress,

$$\sigma(\mathbf{x}, t) = \sigma_f(\mathbf{x}, t) + \sigma_p(\mathbf{x}, t). \quad (7)$$

The Newtonian stress is

$$\sigma_f(\mathbf{x}, t) = -p(\mathbf{x}, t)\mathbb{I} + \frac{\mu_f}{2}(\nabla \mathbf{u}(\mathbf{x}, t) + \nabla \mathbf{u}(\mathbf{x}, t)^\top), \quad (8)$$

in which $p(\mathbf{x}, t)$ is the isotropic pressure and μ_f is the solvent contribution to the viscosity. The viscoelastic fluid models we consider herein can be derived from a microscopic bead-spring model, in which the polymeric stress is linearly related to the conformation tensor by

$$\sigma_p(\mathbf{x}, t) = \frac{\mu_p}{\lambda_r}(\mathbb{C}(\mathbf{x}, t) - \mathbb{I}), \quad (9)$$

in which μ_p is the polymeric contribution to the viscosity, λ_r is the relaxation time of the fluid, and $\mathbb{C}(\mathbf{x}, t)$ is the conformation tensor. The conformation tensor represents an ensemble average over the dyad formed by the local end-to-end vectors characterizing the bead-spring polymers.²⁰ The evolution of the conformation tensor satisfies

$$\overset{\nabla}{\mathbb{C}} = \mathbf{g}(\mathbb{C}(\mathbf{x}, t)), \quad (10)$$

in which $\mathbf{g}(\mathbb{C})$ is the relaxation function of the polymers, which is model dependent, and $\overset{\nabla}{\mathbb{C}}$ is the upper-convected time derivative of \mathbb{C} defined by (1). We consider two models, the Oldroyd-B model

$$\mathbf{g}(\mathbb{C}) = -\frac{1}{\lambda_r}(\mathbb{C} - \mathbb{I}), \quad (11)$$

and the Rolie-Poly model

$$\mathbf{g}(\mathbb{C}) = -\frac{1}{\lambda_d}(\mathbb{C} - \mathbb{I}) - \frac{2}{\lambda_R} \left(1 - \sqrt{\frac{2}{\text{tr}(\mathbb{C})}} \right) \left(\mathbb{C} + \beta \left(\frac{\text{tr}(\mathbb{C})}{2} \right)^\delta (\mathbb{C} - \mathbb{I}) \right), \quad (12)$$

in which λ_d and λ_R are the reptation and Rouse times, respectively, and $\text{tr}(\mathbb{C})$ is the trace of the conformation tensor. In the context of the Rolie-Poly model, we take the relaxation time λ_r in equation (9) to be the reptation time. The parameters β and δ are chosen empirically through a fitting procedure.

The two relevant dimensionless parameters for viscoelastic flow are the Reynolds number, $\text{Re} = \frac{\rho UL}{\mu}$, and the Weissenberg number, $\text{Wi} = \frac{UL}{\lambda_r}$, in which U is a characteristic flow speed and L is a characteristic length scale. The Reynolds number is a ratio between the viscous and inertial forces, and in the applications considered herein, we focus on the small Reynolds number regime relevant for experiments and biological applications of interest. The Weissenberg number is the ratio between the strain rate and the relaxation time of the polymers and represents the ratio of elastic to viscous forces.

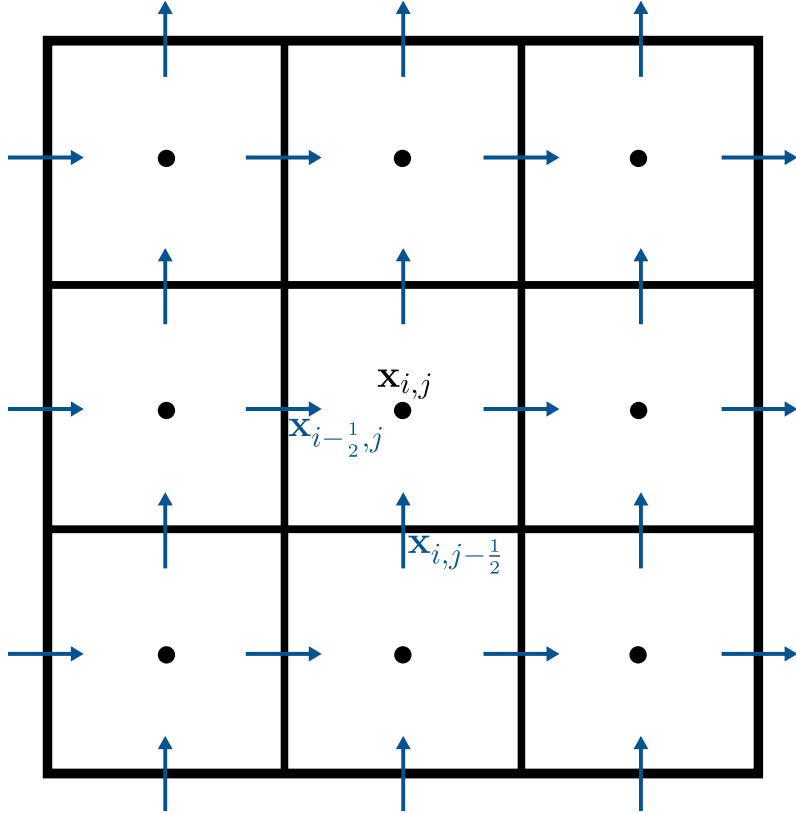


Figure 1: Locations of cell-centered and face-centered quantities about Cartesian grid cell $\mathbf{x}_{i,j}$.

3 Numerical Implementation

This section describes the spatial and temporal discretization of the variables and differential operators involved in equations (2), (3), (5), (4), and (10). Additionally, we comment on the adaptation of our spatial discretization to locally refined Cartesian grids which are implemented in the Oldroyd-B flow past a cylinder benchmark located in section 4.2. The spatial discretization is described in two spatial dimensions and its extension to three spatial dimensions is straightforward. We conclude this section by referencing the software employed in this study and by discussing the appropriate scaling of stiffness parameter κ in equation (3.6) to maintain stability of the discrete system under spatio-temporal grid refinement.

3.1 Spatial Discretization

The working physical domain Ω is described by a fixed $N \times N$ Cartesian grid with uniform meshwidths $\Delta x = \Delta y = h = \frac{L}{N}$, in which L is some chosen characteristic length scale. The Eulerian variables are discretized on a staggered-grid in which the components of the velocity are associated with the grid cell faces and the pressure and conformation tensor degrees of freedom are associated with the grid cell centers. See Figure 1.

We denote centers of the Cartesian grid cells are located at the points $\mathbf{x}_{i,j} = ((i + \frac{1}{2})h, (j + \frac{1}{2})h)$, for $i, j = 0, \dots, N - 1$. The centers of the x -edges of the grid cells are the points $\mathbf{x}_{i-\frac{1}{2},j} = (ih, (j + \frac{1}{2})h)$, where $i = 0, \dots, N$ and $j = 0, \dots, N - 1$. The centers of the y -edges are the points $\mathbf{x}_{i,j-\frac{1}{2}} = ((i + \frac{1}{2})h, jh)$, for $i = 0, \dots, N - 1$ and $j = 0, \dots, N$. The pressure $p(\mathbf{x}, t)$ and conformation tensor \mathbb{C} are defined at the centers of the Cartesian grid cells. The horizontal component, u , of the velocity is defined on the x -edges of the grid cells and the vertical component of the velocity, v , is defined along the y -edges of the grid cells. The horizontal component and vertical components of the force are likewise defined along the x -edges and y -edges of the grid cells, respectively.

We now detail the discretization of the spatial differential operators present in the Eulerian equations of motion.

Standard compact second-order finite differences are used for the divergence and Laplacian of the velocity and the gradient of the velocity.⁴² The Laplacian of the velocity $\nabla_h^2 \mathbf{u}$ and the pressure gradient $\nabla_h p$ are evaluated at cell faces, and the divergence of the velocity $\nabla_h \cdot \mathbf{u}$ is evaluated at cell centers. The convective operator in the momentum equation (2) and the evolution of the conformation tensor (10) is approximated using a piecewise parabolic method (PPM) approach based off the xsPPM7 scheme.⁴³ We also require finite difference stencils for the divergence of the conformation tensor $\nabla_h \cdot \mathbb{C}$ at cell faces and the velocity gradient $\nabla_h \mathbf{u}$ at cell centers. Finite difference stencils are needed for the divergence of the conformation tensor, since, in practice, we replace the divergence of the polymeric stress present in equation (2) with the divergence of the conformation tensor as per equation (9).

To approximate the velocity gradient, we use

$$\left(\frac{\partial u}{\partial x} \right)_{i,j} \approx \frac{u_{i+\frac{1}{2},j} - u_{i-\frac{1}{2},j}}{h}, \quad (13)$$

$$\left(\frac{\partial u}{\partial y} \right)_{i,j} \approx \frac{u_{i+\frac{1}{2},j+1} + u_{i-\frac{1}{2},j+1} - u_{i+\frac{1}{2},j-1} - u_{i-\frac{1}{2},j-1}}{4h}, \quad (14)$$

$$\left(\frac{\partial v}{\partial x} \right)_{i,j} \approx \frac{v_{i+1,j+\frac{1}{2}} + v_{i+1,j-\frac{1}{2}} - v_{i-1,j+\frac{1}{2}} - v_{i-1,j-\frac{1}{2}}}{4h}, \quad (15)$$

$$\left(\frac{\partial v}{\partial y} \right)_{i,j} \approx \frac{v_{i,j+\frac{1}{2}} - v_{i,j-\frac{1}{2}}}{h}. \quad (16)$$

For the divergence of the conformation tensor arising in equation (2), we use the following stencils

$$\left(\frac{\partial C_{xx}}{\partial x} \right)_{i-\frac{1}{2},j} \approx \frac{C_{xx_{i,j}} - C_{xx_{i-1,j}}}{h}, \quad (17)$$

$$\left(\frac{\partial C_{xy}}{\partial y} \right)_{i-\frac{1}{2},j} \approx \frac{C_{xy_{i+1,j+1}} + C_{xy_{i-1,j+1}} - C_{xy_{i+1,j-1}} - C_{xy_{i-1,j-1}}}{4h}, \quad (18)$$

$$\left(\frac{\partial C_{yx}}{\partial x} \right)_{i,j-\frac{1}{2}} \approx \frac{C_{yx_{i+1,j+1}} + C_{yx_{i+1,j-1}} - C_{yx_{i-1,j+1}} - C_{yx_{i-1,j-1}}}{4h}, \quad (19)$$

$$\left(\frac{\partial C_{yy}}{\partial y} \right)_{i,j-\frac{1}{2}} \approx \frac{C_{yy_{i,j}} - C_{yy_{i,j-1}}}{h}. \quad (20)$$

We note that the stencils above represent a centered, formally second-order accurate approximation of both the velocity gradient and divergence of the conformation tensor.

3.1.1 Locally Refined Cartesian Grids

This section briefly describes the locally refined Cartesian grid strategy employed in section 4.2 to simulate the flow of an Oldroyd-B fluid past a stationary cylinder. For a static locally refined grid, the physical domain Ω is decomposed into a union of rectangular grid patches. Each rectangular grid patch is organized into a sequence of locally refined patch levels which we call the patch hierarchy. The levels are numbered $l = 0, \dots, l_{\max}$, in which $l = 0$ and l_{\max} indicate the coarsest and finest levels in the patch hierarchy, respectively. All of the grid patches associated to a particular refinement level l have the same Cartesian grid increments $(\Delta x_l, \Delta y_l)$. In the context of the present paper, we specialize to the case $\Delta x_l = \Delta y_l = h_l$. The grid increment at a particular level h_l is specified to be an integer multiple of the grid increment at level $l+1$, so that $h_{l+1} = rh_l$ for some positive integer $r > 0$. For the Oldroyd-B flow past a stationary cylinder example, we set the integer ratio of refinement $r = 2$ and use a total of four refinement levels. Figure 2 illustrates the static grid utilized for the Oldroyd-B flow past a stationary cylinder example discussed in section 4.2.

— Level 0 ($h_0 = 1$ (mm)) — Level 2 ($h_2 = \frac{1}{4}$ (mm))
— Level 1 ($h_1 = \frac{1}{2}$ (mm)) — Level 3 ($h_3 = \frac{1}{8}$ (mm))

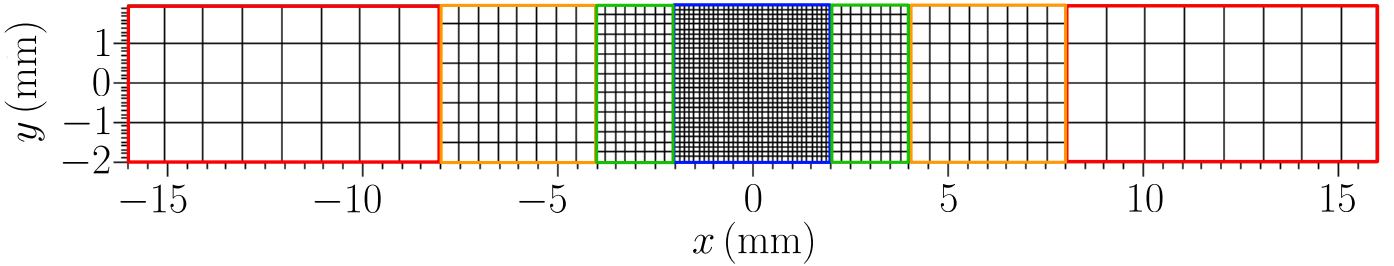


Figure 2: A coarser version of the statically refined grid used in the Oldroyd-B flow past a cylinder example in section 4.2.

Each grid cell on a particular level l of the patch hierarchy is either entirely covered by grid cells on the next finest level $l+1$ or is not covered at all. The Eulerian variables \mathbf{u} , p , and \mathbb{C} are discretized as described in section 3.1 on each level of the patch hierarchy and are considered *composite grid variables*. For such variables, their degrees of freedom are defined only on regions of the patch hierarchy that belong to their corresponding resolution or a coarser one. The values of the variable defined on finer regions of the patch hierarchy are defined implicitly through a conservative averaging procedure which is described by Griffith et al.⁷ The divergence, gradient, and Laplacian operators are approximated on each level of the patch hierarchy using standard centered second-order finite difference stencils defined in section 3.1 above. Near coarse-fine interfaces, ghost cell values must be supplied to the stencils of each finite difference operator. The ghost-cell filling procedures are described in detail by Griffith et al.⁷

3.2 Lagrangian grid spacing

The reference configuration Γ_0 of each immersed boundary we consider in section 4 is made up of a finite collection of open or closed smooth curves. Each curve comprising Γ_0 can be expressed by a parametrization $\mathbf{X}(s)$ which we discretize by placing a finite number M of Lagrangian markers located at $\{\mathbf{X}(s_k)\}_{k=1}^{k=M}$ along the curve in which we take s_1 to be the infimum over the set where s takes its values. The Lagrangian markers are placed along each curve to ensure that the arc length increment, ΔX_k , defined by

$$\Delta X_k = \int_{s_k}^{s_{k+1}} \left\| \frac{d\mathbf{X}_k(s')}{ds'} \right\|_2 ds' \quad (21)$$

remains approximately equal to an a priori chosen idealized arc length increment ΔX . It is often the case that the total arc length L of a curve $\mathbf{X}(s)$ making up Γ_0 is not an integer multiple of the ideal arc length increment ΔX . In this situation, if the curve parameterized by $\mathbf{X}(s)$ is closed, we first compute $M = \lfloor \frac{L}{\Delta X} \rfloor$, in which $\lfloor \cdot \rfloor$ is the function which rounds to the nearest integer, and set $\Delta X = \frac{L}{M}$. We then place Lagrangian markers along $\mathbf{X}(s)$ starting at $\mathbf{X}(s_1)$ and then at $\mathbf{X}(s_{k+1})$ by solving

$$\int_{s_k}^{s_{k+1}} \left\| \frac{d\mathbf{X}(s')}{ds'} \right\|_2 ds' - \Delta X = 0, \quad (22)$$

for s_{k+1} and $k = 1, \dots, M-1$. In the case in which the curve $\mathbf{X}(s)$ is open, we still set $M = \lfloor \frac{L}{\Delta X} \rfloor$, but choose the ideal arc length increment to be $\Delta X = \frac{L}{M-1}$. We then follow the same procedure and place a Lagrangian marker starting at $\mathbf{X}(s_1)$ and solve equation (22) for the remaining locations of the Lagrangian markers $\mathbf{X}(s_{k+1})$ for $k = 1, \dots, M-1$. With our discretization procedure in place, we next define the mesh factor, M_{fac} , to be the ratio of the idealized arc length increment ΔX to the finest Eulerian grid mesh width h , i.e.

$$M_{\text{fac}} = \frac{\Delta X}{h}. \quad (23)$$

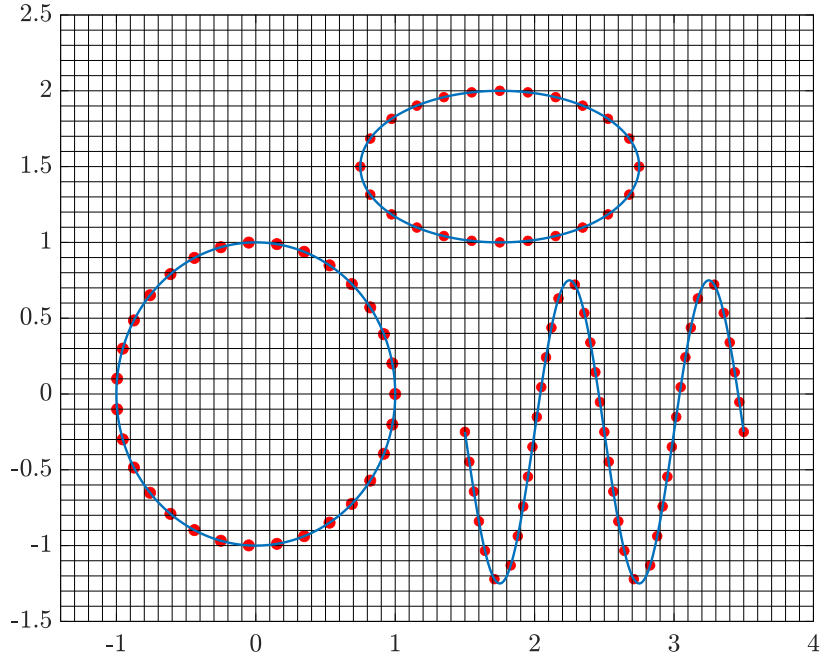


Figure 3: Example Lagrangian discretization of a circle, ellipse, and a sine curve. Here $h = 0.1$ and the mesh factor is $M_{\text{fac}} = \frac{\Delta X}{h} = 2$, in which ΔX is the ideal arc length increment separating each Lagrangian marker along a curve. Since the total arc length of each curve is not necessarily an integer multiple of the Cartesian grid increment, the total number of Lagrangian markers placed along each curve is obtained by rounding the ratio of the total arc length of a curve to the ideal arc length increment to the nearest integer. When the arc length of a given curve is not an explicitly invertible function, Lagrangian markers are placed along the curve by approximately inverting the arc length function through the use of a nonlinear solver with an error tolerance specified to be at least three orders of magnitude smaller than the idealized arc length increment.

To construct the initial configuration of the immersed boundary Γ_0 , we choose the ideal arc length increment ΔX based on a particular choice of M_{fac} . To illustrate, suppose we set $M_{\text{fac}} = 2$ and choose Γ_0 to be made up of a circle of radius $r = 1$ and with center $(0, 0)$, an ellipse with center $(1.75, 1.5)$, width 2, and height 1, and a sine curve of frequency 2π and mean amplitude -0.25 starting at $x = 1.5$ and ending at $x = 3.5$. The parameterizations of these curves are $\mathbf{X}_1 = (\cos(s_1), \sin(s_1))$ with $s_1 \in [0, 2\pi]$, $\mathbf{X}_2 = (1.75 + \cos(s_2), 1.5 + \sin(s_2))$ with $s_2 \in [0, 2\pi]$, and $\mathbf{X}_3 = (s_3, -0.25 + \sin(2\pi s_3))$ with $s_3 \in [1.5, 3.5]$, respectively. Following our discretization procedure above, we produce the discretization of Γ_0 shown in Figure 3.

3.3 Spreading and Interpolation

The interaction between the fluid and structure is mediated by the equations (4) and (5). In the IB method, the singular delta functions supported on the immersed boundary are replaced by regularized delta functions $\delta_h(x)$. Given the Lagrangian force $\mathbf{F}(\mathbf{X}, t) = (F_1(\mathbf{X}, t), F_2(\mathbf{X}, t))$, the forces $\mathbf{f}(\mathbf{x}, t) = (f_1(\mathbf{x}, t), f_2(\mathbf{x}, t))$ on the Cartesian grid are computed as

$$(f_1)_{i-\frac{1}{2},j} = \sum_{I=1}^M F_1(\mathbf{X}_I, t) \delta_h(\mathbf{x}_{i-\frac{1}{2},j} - \chi(\mathbf{X}_I, t)) \Delta \mathbf{X}_I, \quad (24)$$

$$(f_2)_{i,j-\frac{1}{2}} = \sum_{I=1}^M F_2(\mathbf{X}_I, t) \delta_h(\mathbf{x}_{i,j-\frac{1}{2}} - \chi(\mathbf{X}_I, t)) \Delta \mathbf{X}_I, \quad (25)$$

in which M is the total number of Lagrangian points and $\Delta\mathbf{X}_I$ is the arc-length element associated with Lagrangian grid point \mathbf{X}_I , which is described in section 3.2. We denote the spreading operation of the force onto the background grid as

$$\mathbf{f}(\mathbf{x}, t) = \mathcal{S}[\chi](\mathbf{x}, t), \quad (26)$$

in which \mathcal{S} is the force spreading operator. The velocity of the structure in equation 5 is approximated by

$$\mathbf{U}(\mathbf{X}, t) = \mathcal{I}[\chi](\mathbf{X}, t), \quad (27)$$

in which \mathcal{I} is the interpolation operator. We construct the interpolation operator by requiring that it be adjoint to the spreading operator, $\mathcal{I} = \mathcal{S}^*$. This requirement is fulfilled by using the same regularized delta functions to both spread forces onto the background grid and interpolate velocities onto the immersed structure.

3.4 Regularized Delta Functions

The computational tests in section 4 explore the impact of the form of the regularized delta function on the accuracy of the numerical method. We consider five different constructions of δ_h . Each construction is of a tensor-product form, so that

$$\delta_h(\mathbf{x}) = \frac{1}{h^2} \phi\left(\frac{x_1}{h}\right) \phi\left(\frac{x_2}{h}\right), \quad (28)$$

for different choices of one-dimensional kernel functions $\phi(r)$. The regularized delta functions we utilize are derived from two different families of one-dimensional kernel functions ϕ . The first two kernel functions are the linear and quadratic members of the B-spline family. We refer to these kernel functions below as the piecewise-linear and three-point B-splines, respectively. The piecewise-linear B-spline kernel is the least regular of all the kernel functions considered in this study and is continuous but not differentiable. The three-point B-spline kernel is continuously differentiable. The discovery of the B-spline family of kernel functions is attributed to Schoenberg,⁴⁴ however, even Schoenberg himself noted that Hermite, Peano, and Laplace were all well aware of B-splines.⁴⁵ The other three kernel functions we consider belong to the so called IB family of kernel functions. The IB family of kernel functions were conceived by Peskin, who postulated the properties the IB family ought to satisfy to be computationally efficient, accurate, physical, and mathematically simple.¹ In this work, we use the three-point, four-point, and Gaussian-like six-point IB kernel functions. The three-point IB kernel was originally introduced in an adaptive version of the IB method in which the Eulerian components were discretized on a staggered-grid.³⁰ The four-point IB kernel is the most commonly used and satisfies all of Peskin's original postulates.¹ The Gaussian-like six-point IB kernel was formulated more recently⁴⁶ and is the smoothest kernel function we use as it is three times continuously differentiable. The four-point and three-point IB kernels are both continuously differentiable. Figure 4 displays each of the one dimensional kernel functions $\phi(r)$ we consider in this work.

3.5 Temporal Discretization

We discretize in time using a modified trapezoidal rule for the momentum equation and incompressibility constraint, the midpoint rule for the immersed boundary, and an explicit trapezoidal rule for the evolution of the conformation tensor. Specifically, to advance from time t^n to time $t^{n+1} = t^n + \Delta t$, we first compute an approximation to the position of the immersed boundary and the conformation tensor at time t^{n+1} ,

$$\tilde{\chi}^{n+1} = \chi^n + \Delta t \mathcal{I}[\chi^n] \mathbf{u}^n, \quad (29)$$

$$\frac{\tilde{\mathbb{C}}^{n+1} - \mathbb{C}^n}{\Delta t} + \mathbb{N}_2^n = \nabla_h \mathbf{u}^n \mathbb{C}^n + \mathbb{C}^n (\nabla_h \mathbf{u}^n)^\top + \mathbf{g}(\mathbb{C}^n), \quad (30)$$

in which \mathbb{N}_2^n is an approximation of the advection term $\mathbf{u}^n \cdot \nabla \mathbb{C}^n$. We then compute the Lagrangian force at the mid-time point $t^{n+\frac{1}{2}}$,

$$\mathbf{F}^{n+\frac{1}{2}} = \kappa \left(\chi^0 - \frac{\tilde{\chi}^{n+1} + \chi^n}{2} \right). \quad (31)$$

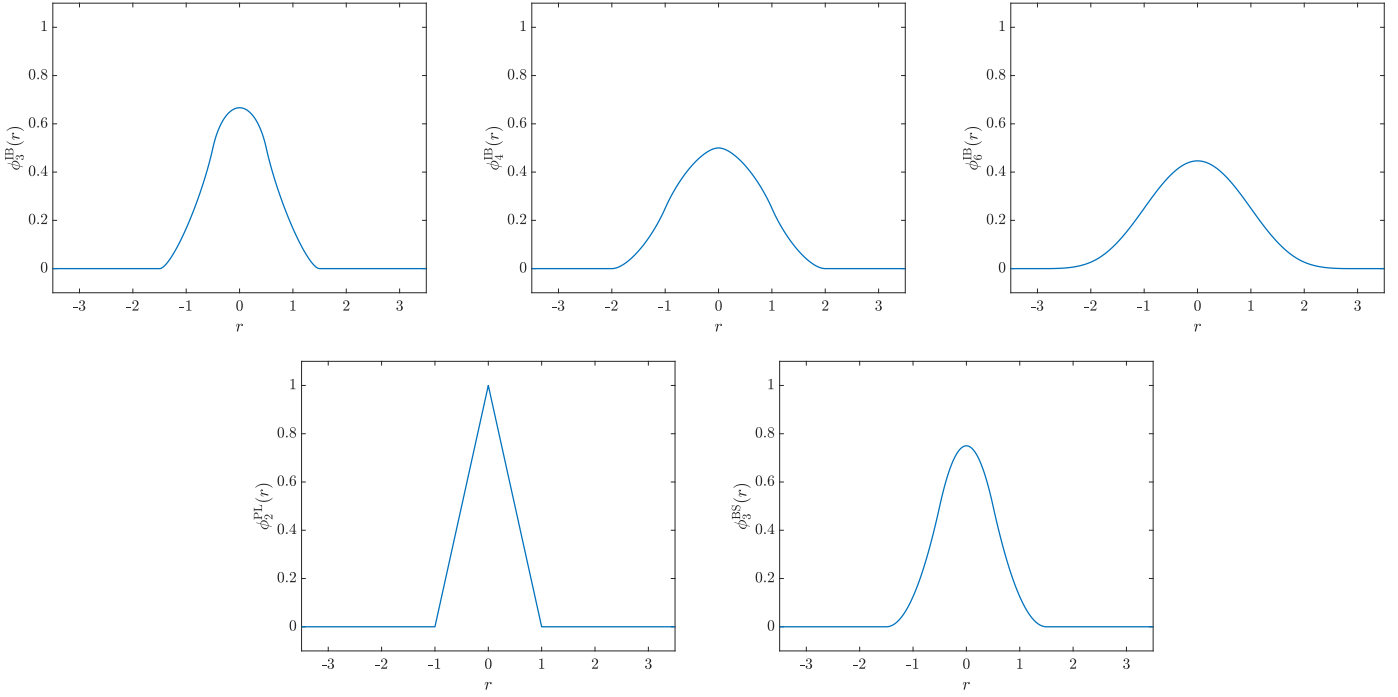


Figure 4: Illustrations of the kernel functions used to construct the regularized delta functions employed in this work. On the top from left to right are the three-point, four-point, and Gaussian-like six-point IB kernel functions. Below from left to right are the piecewise linear and three-point B-spline kernel functions.

We then compute the new velocity and pressure,

$$\frac{\mathbf{u}^{n+1} - \mathbf{u}^n}{\Delta t} + \frac{3}{2} \mathbf{N}_1^n - \frac{1}{2} \mathbf{N}_1^{n-1} = -\nabla_h p^{n+\frac{1}{2}} + \mu_f \nabla_h^2 \frac{\mathbf{u}^{n+1} + \mathbf{u}^n}{2} + \frac{\mu_p}{\lambda_r} \nabla_h \cdot \left(\frac{\tilde{\mathbb{C}}^{n+1} + \mathbb{C}^n}{2} \right) + \mathcal{S} \left[\chi^{n+\frac{1}{2}} \right] \mathbf{F}^{n+\frac{1}{2}}, \quad (32)$$

$$\nabla_h \cdot \mathbf{u}^{n+1} = 0, \quad (33)$$

in which \mathbf{N}_1^n is an approximation of the advective term $\mathbf{u}^n \cdot \nabla \mathbf{u}^n$. This linear system is solved by a GMRES solver which applies the projection method as a preconditioner.⁴² Finally, we compute the conformation tensor and the immersed boundary position at time t^{n+1} using an explicit trapezoidal rule and midpoint rule respectively,

$$\frac{\mathbb{C}^{n+1} - \mathbb{C}^n}{\Delta t} + \frac{1}{2} \left(\mathbb{N}_2^n + \mathbb{N}_2^{n+1} \right) = \frac{1}{2} \left(\nabla_h \mathbf{u}^n \mathbb{C}^n + \mathbb{C}^n (\nabla_h \mathbf{u}^n)^\top \right) + \frac{1}{2} \left(\nabla_h \mathbf{u}^{n+1} \tilde{\mathbb{C}}^{n+1} + \tilde{\mathbb{C}}^{n+1} (\nabla_h \mathbf{u}^{n+1})^\top \right) + \frac{1}{2} \left(\mathbf{g}(\mathbb{C}^n) + \mathbf{g}(\mathbb{C}^{n+1}) \right), \quad (34)$$

$$\chi^{n+1} = \chi^n + \Delta t \mathcal{J} \left[\chi^{n+\frac{1}{2}} \right] \mathbf{u}^{n+\frac{1}{2}}, \quad (35)$$

in which $\mathbf{u}^{n+\frac{1}{2}} = \frac{1}{2} (\mathbf{u}^n + \mathbf{u}^{n+1})$ and \mathbb{N}_2^{n+1} is an approximation of $\mathbf{u}^{n+1} \cdot \nabla \tilde{\mathbb{C}}^{n+1}$. We note that each time step requires the solution of the Navier-Stokes equations, one force evaluation, and two velocity spreading operations.

3.6 Choice of the Spring Penalty Parameter κ

In practice, the spring stiffness parameter κ is determined to be the smallest value that keeps the Lagrangian markers from moving a Euclidean distance of more than $\frac{h}{2}$ from their initial position. When implementing convergence tests, we scale the stiffness parameter according to $\kappa = C \frac{h}{\Delta t^2}$ in which C is a constant which is determined by finding the working κ value for the coarsest discretization chosen. There are two reasons to scale κ in this way: first, the scaling

is consistent with the physical units of a linear spring; and second, it has been demonstrated in both by Lai⁴⁷ and by Hua and Peskin⁴⁸ that this scaling of κ maintains the numerical stability of the IB system of equations in the context of the Navier-Stokes equations. In the viscoelastic fluids simulations carried out here, we also observe that this scaling κ maintains the stability of our numerical scheme when making refinements to the grid and time step size.

3.7 Definition of Discrete L^p norms

To empirically analyze the convergence properties of the IB method, we make use of discrete L^p norms. The discrete L^p norms used herein are the same as the ones defined by Griffith et al.⁴⁹

3.8 Software Implementation

The solvers are implemented in IBAMR,⁵⁰ which is an MPI-parallelized implementation of the immersed boundary method. Support for structured adaptive mesh refinement is provided by SAMRAI,^{51,52} and the linear solvers are implemented using PETSc.⁵³⁻⁵⁵

4 Numerical Tests

We use the IB method to model the flow of a viscoelastic fluid through or around a stationary structure. The rigidity of the structure is weakly imposed using the penalty spring forcing approach as described in section 2. Initially, the viscoelastic fluid is assumed to be at rest and the dynamics of the flow are driven by the specification of inflow and outflow velocity boundary conditions. For each test, the simulation is allowed to proceed until steady-state conditions are reached. We found empirically that steady-state conditions are achieved when the duration of the simulation exceeds twenty times the size of the relaxation number λ_r in the case of an Oldroyd-B fluid, or twenty times the size of the reptation time λ_d in the case of a Rolie-Poly fluid. Additionally, for each numerical test, we perform a grid convergence study and estimate rates of convergence either by comparing our computed solution to an analytic steady-state solution when available, or by utilizing Richardson extrapolation. When refinements to the grid are made, the timestep size and penalty spring parameter κ are scaled consistently to ensure the stability of our numerical scheme. The timestep size is scaled as some constant multiplied by finest Cartesian grid increment, and the penalty spring parameter κ is scaled as described in section 3.6.

4.1 Oldroyd-B Flow Through an Inclined Channel

We begin our series of numerical tests by analyzing Oldroyd-B flow through an inclined channel. The channel was chosen to be inclined rather than completely vertical or horizontal to avoid having a completely grid aligned discretization of the channel walls. To assess the accuracy of our numerical simulations, we simulate startup Oldroyd-B channel flow using the steady-state solution for Oldroyd-B channel flow as the inflow boundary condition and allow the simulation to proceed until a given simulation until steady state is reached. The absolute error associated with our steady-state solution is then computed in the L^1 , L^2 , and L^∞ grid norms.

Assuming a constant pressure gradient of unit magnitude, the analytic steady-state solution to Oldroyd-B flow through the inclined channel is

$$u(x, y) = -\frac{\cos \theta}{2(\mu_s + \mu_p)} (y \cos \theta - x \sin \theta) (y \cos \theta - x \sin \theta - H), \quad (36)$$

$$v(x, y) = -\frac{\sin \theta}{2(\mu_s + \mu_p)} (y \cos \theta - x \sin \theta) (y \cos \theta - x \sin \theta - H), \quad (37)$$

$$C_{xx}(x, y) = \cos^2 \theta \tilde{C}_{xx}(x, y) + \sin^2 \theta \tilde{C}_{yy}(x, y) - 2 \cos \theta \sin \theta \tilde{C}_{xy}(x, y), \quad (38)$$

$$C_{xy}(x, y) = \tilde{C}_{xy}(x, y) (\cos^2 \theta - \sin^2 \theta) + \cos \theta \sin \theta (\tilde{C}_{xx}(x, y) - \tilde{C}_{yy}(x, y)), \quad (39)$$

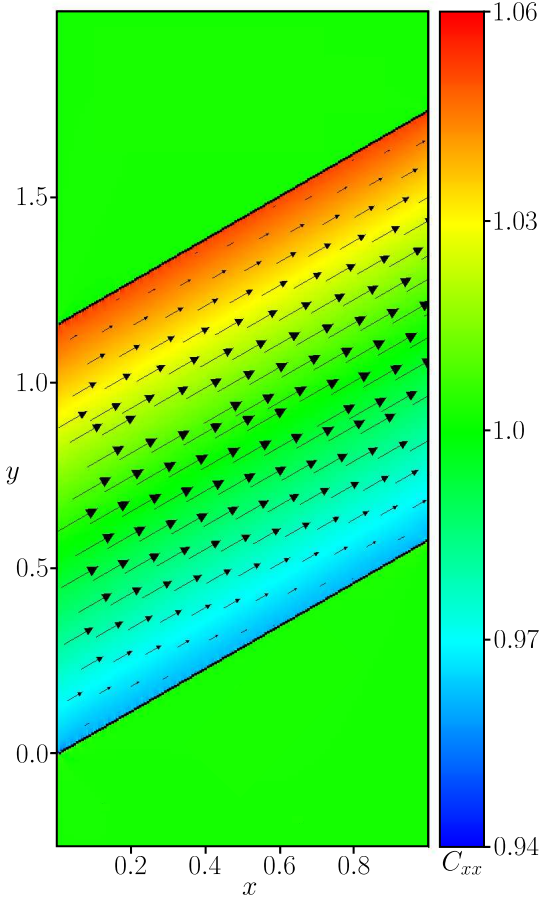


Figure 5: Visualization of the computed steady state solution to Oldroyd-B flow through an inclined channel using piecewise linear kernel with $M_{\text{fac}} = 2.0$, $\mu_s = \mu_p = 0.5$, $\theta = \frac{\pi}{6}$, and $\lambda = 0.1$ on the finest uniform grid ($h = \frac{1}{512}$). The velocity vector field (in black) is illustrated alongside the (1,1) component of the dimensionless conformation tensor \mathbb{C} . The units of length are in centimeters. The black dots outlining the channel represent the steady state locations of the Lagrangian markers.

$$C_{yy}(x, y) = \cos^2 \theta \tilde{C}_{yy}(x, y) + \sin^2 \theta \tilde{C}_{xx}(x, y) + 2 \cos \theta \sin \theta \tilde{C}_{xy}(x, y), \quad (40)$$

in which H is the height of the horizontal channel, θ is the angle of rotation of the horizontal channel about the origin, and $\tilde{\mathbb{C}}$ is the conformation tensor associated with the analytic steady state solution for the horizontal channel;

$$\tilde{C}_{xx}(\tilde{x}, \tilde{y}) = 1 + 2\tilde{C}_{xy}(\tilde{y})^2, \quad (41)$$

$$\tilde{C}_{xy}(\tilde{x}, \tilde{y}) = \lambda \frac{\partial u}{\partial \tilde{y}} = -\frac{\lambda}{\mu_s + \mu_p} \left(\tilde{y} - \frac{H}{2} \right), \quad (42)$$

$$\tilde{C}_{yy} = 1. \quad (43)$$

We set $\theta = \frac{\pi}{6}$, $H = 1.0$, $\mu_s = \mu_p = 0.5$, and $\lambda = 0.1$. All simulations are run until a final time of $T_{\text{final}} = 20\lambda = 2.0$ s to ensure that steady state is approximately reached. For each choice of regularized delta function and M_{fac} value, we perform a total of four simulations on increasingly fine uniform grids $h = \frac{1}{32}, \frac{1}{64}, \frac{1}{128}$, and $\frac{1}{256}$. The time step size for each discretization is chosen to be $\Delta t = 0.2h$, and the stiffness parameter κ is set to $\kappa = 10 \frac{h}{\Delta t^2}$. Figure 5 shows a representative solution. Figure 6 analyzes the impact of M_{fac} on the accuracy of the computed solution. The accuracy of the computed solution appears to be independent of the working M_{fac} value chosen. However, we observe that the use of regularized delta functions with narrower supports provide more accurate solutions at comparable grid resolutions than regularized delta functions of broader support. At first, this finding may seem somewhat surprising since all

the regularized delta functions employed satisfy the same discrete moment conditions, which should make them all approximately equally accurate interpolants of *smooth* functions. However, the velocity we are approximating with the IB method is not a smooth function — the true velocity has a discontinuous jump in its normal derivative across the immersed boundary.⁵⁶ The discrepancies in errors across different regularized delta functions can be explained, at least heuristically, by considering the interpolation error associated with a function whose normal derivative has a jump discontinuity at the interpolation point of interest. In spatial variable, the leading order error term is precisely the mean value of the regularized delta function on half space multiplied the value of the jump in the derivative. This finding was applied originally by Beyer and Leveque²² to derive a second-order accurate one-dimensional version of the IB method. Consequently, regularized delta functions with narrower supports (and hence smaller mean values on half space) will provide more accurate interpolations of a velocity that is C^0 but not C^1 the point of interest. In the context of this study, we note that the half space mean value of the six point IB kernel is approximately twice that of the piecewise linear kernel, and, as Figure 6 demonstrates, the error in the computed velocity using the six-point IB regularized delta function is approximately twice that of the piecewise-linear regularized delta function.

Figure 7 analyzes the global convergence properties of the IB method applied to the Oldroyd-B flow through an inclined channel the particular value of $M_{\text{fac}} = 2$. In general, we find that the velocity converges at a first-order rate for each of the grid norms used while the components of the conformation tensor converge at about a first-order rate in L^1 , a half-order rate in L^2 , and fails to converge in L^∞ . The convergence rates for the other M_{fac} values tested were consistent with these results. The conformation tensor's lack of pointwise convergence is a consequence of the lack of pointwise convergence of the velocity gradients in the IB method. Nonetheless, as demonstrated in section 4.2, the viscoelastic IB method is still able to capture convergent *net forces* on the immersed structures.

4.2 Oldroyd-B Flow Past a Cylinder

Next, we utilize the IB method to study the problem of Oldroyd-B flow past a confined and stationary cylinder. In the literature, this problem is typically studied in the zero Reynolds number limit and so the evolution of the extra-stress or conformation tensor is coupled to the steady state Stokes equations rather than the full Navier-Stokes equations.^{39,57-59} However, our discretization near coarse-fine interfaces limits the solvers used herein to non-zero Reynolds numbers. Therefore, we perform the following simulations at the Reynolds number of $\text{Re} = 1.0 \times 10^{-5}$ to make comparisons to literature values. The radius of the cylinder is set to $R = 1$ for each of our numerical tests. Our working computational domain is $\Omega = [-L/2, L/2] \times [-H/2, H/2]$ with $L = 32R$ and $H = 4R$. Each of our simulations run until $T_{\text{final}} = 20\lambda$ so that a steady state solution is achieved.

To assess the accuracy of our numerical simulations, we compute convergence rates of the velocity, conformation tensor, and pressure fields and also compute the steady-state drag coefficient. We shall only focus on the well studied low Weissenberg number case $\text{Wi} = 0.1$, for which the agreed upon literature value is approximately $C_d = 130.364$.³⁹ To compute the steady-state drag coefficient, we follow the method employed in by Stein et al.³⁹ and compute the steady-state drag coefficient by a discretization of

$$C_d = -\frac{\mu_s}{\mu_s + \mu_p} \int_{\Gamma} \mathbf{F}(\mathbf{X}) \cdot \hat{\mathbf{x}} \, dA, \quad (44)$$

in which $\hat{\mathbf{x}}$ is the unit vector pointing in the x -direction. We compute the drag in this a way to avoid computing a surface integral defined in terms of the stress because, as mentioned above, the conformation tensor and the extra stress tensor are not expected converge along immersed boundaries when using the IB method. Table 1 reports the relative errors in the computed drag coefficients for each kernel and M_{fac} value tested. In particular, we observe that for each of the regularized delta functions tested, the computed drag coefficient appears to converge at a first-order rate, indicating that the IB method is capable of computing accurate net forces on immersed boundaries as long as the grid resolution is fine enough. In addition, similar to Oldroyd-B flow through the inclined channel above, we observe that for the finest resolution cases, across all M_{fac} values tested, using regularized delta functions of narrower support tends to lead to more accurate computations of drag coefficient. However, we also observe that the accuracy of the computed drag coefficient appears much more sensitive to the M_{fac} value for regularized delta functions of narrower

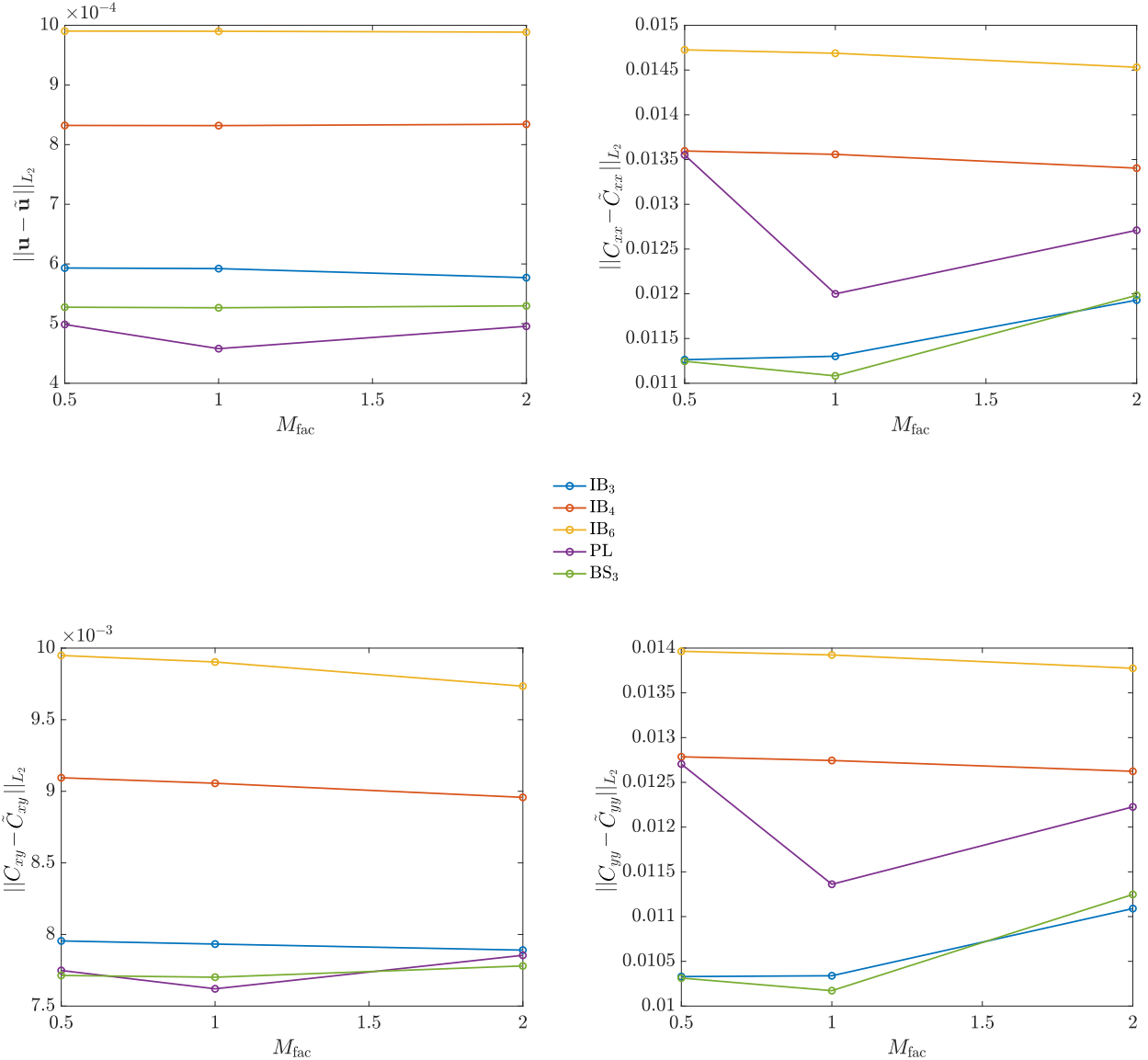


Figure 6: Plots of L^2 grid errors at the intermediate discretization of $h = \frac{1}{128}$ for working M_{fac} values of $\frac{1}{2}, 1$, and 2 . For each M_{fac} value tested, the computed steady state values of the velocity $\tilde{\mathbf{u}}$ and the conformation tensor $\tilde{\mathbb{C}}$ were computed and compared against their respective analytic solutions for Oldroyd-B flow through a channel. We observe that the L^2 error is independent of the M_{fac} values tested. The error dependence on the M_{fac} values tested in the L^∞ and L^1 norms are analogous.

support. Preliminary results indicate that the sensitivity in the accuracy of the drag coefficient associated with the M_{fac} value chosen is not primarily influenced by the presence of a viscoelastic fluid. Rather, it appears to be inherent to the IB method itself.

We remark that for the finest grid resolution tested ($h_{\text{finest}} = \frac{1}{64}$), using the piecewise-linear regularized delta function with $M_{\text{fac}} = 2$ or the three-point B-spline regularized delta function at any of the M_{fac} values tested, results in drag coefficients whose relative errors are on the same order of magnitude as those computed using the finite element discretization described by Tenchev et al.⁶⁰ for a comparably resolved mesh. In addition, Tenchev et al. also observed that the drag coefficient obtained using their finite element implementation converged at an approximately first-order rate.⁶⁰

To complement our analysis of Oldroyd-B flow past a cylinder, Table 2 shows the empirical global rates of conver-

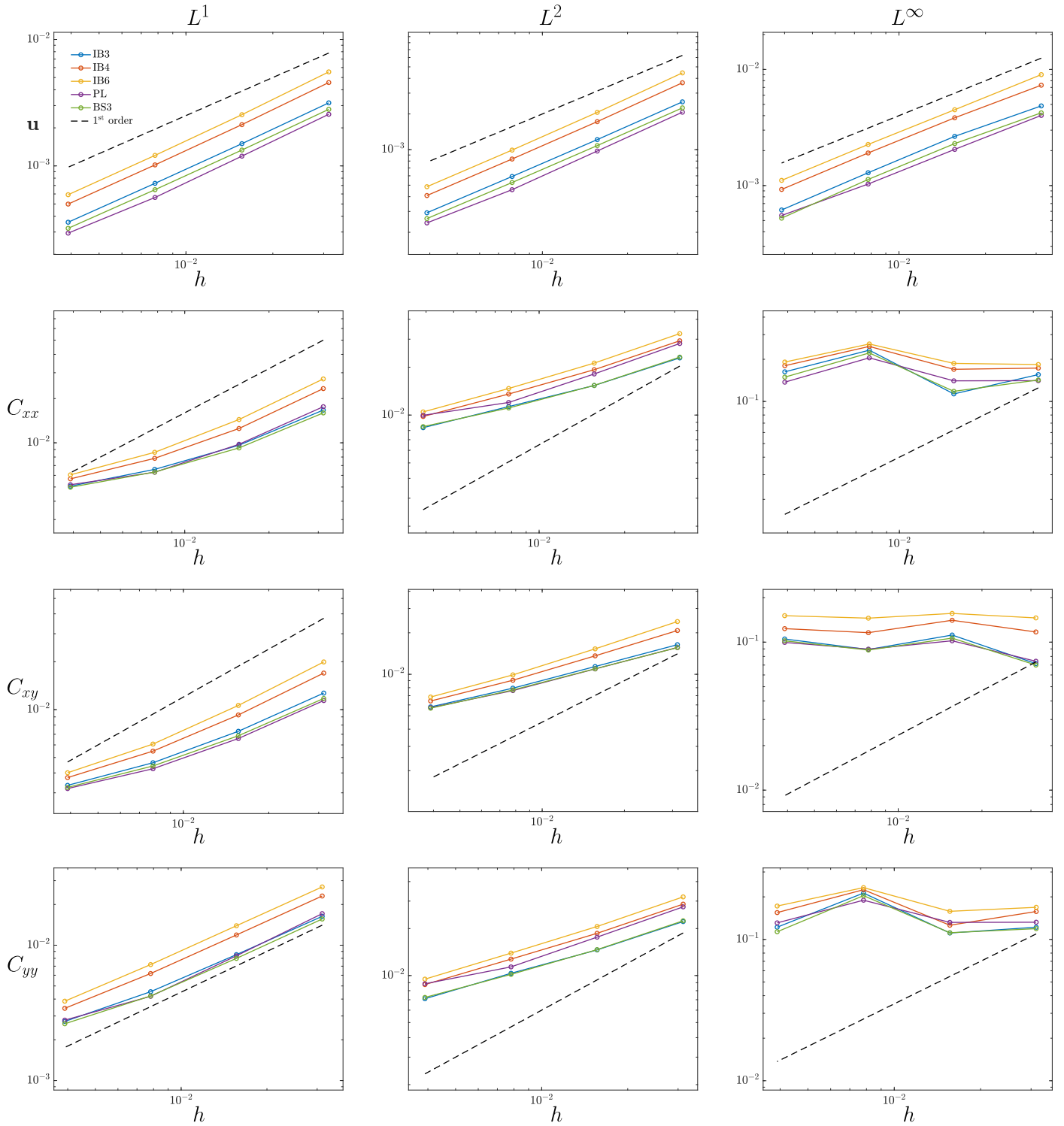


Figure 7: Log-log plots analyzing the convergence properties of the steady-state velocity and components of the conformation tensor for Oldroyd-B flow through an inclined channel simulated using the IB method with an M_{fac} value of 2. We observe first-order convergence in all grid norms for the components of the velocity and approximately first-order convergence in the L^1 norm, a half-order of convergence in the L^2 norm, and the failure of convergence in the L^∞ norm for each component of the conformation tensor. Convergence results for the other M_{fac} values tested were similar.

gence of the velocity, stress tensor, and pressure computed using the three-point B-spline kernel with an M_{fac} of $\frac{1}{2}$. Empirical rates for other regularized delta functions and choices of M_{fac} are similar. Below Table 2, we present the

Table 1: Relative Errors in the computed drag coefficient C_d for Oldroyd-B flow past a stationary cylinder for each of the regularized delta functions and M_{fac} values tested.

$M_{\text{fac}} = \frac{1}{2}$	BS3	IB3	PL	IB4	IB6
$h_{\text{finest}} = \frac{1}{16}$	6.15%	9.55%	12.92%	10.50%	11.16%
$h_{\text{finest}} = \frac{1}{32}$	2.78%	4.11%	5.39%	4.73%	5.02%
$h_{\text{finest}} = \frac{1}{64}$	1.39%	2.04%	2.71%	2.32%	2.38%
<hr/>					
$M_{\text{fac}} = 1$					
$h_{\text{finest}} = \frac{1}{16}$	5.45%	6.20%	4.77%	9.51%	11.16%
$h_{\text{finest}} = \frac{1}{32}$	2.61%	2.92%	2.54%	4.37%	5.02%
$h_{\text{finest}} = \frac{1}{64}$	1.24%	1.42%	1.19%	2.07%	2.38%
<hr/>					
$M_{\text{fac}} = 2$					
$h_{\text{finest}} = \frac{1}{16}$	4.57%	5.86%	1.57%	9.06%	11.16%
$h_{\text{finest}} = \frac{1}{32}$	2.12%	2.66%	1.03%	4.16%	5.02%
$h_{\text{finest}} = \frac{1}{64}$	1.01%	1.28%	0.46%	1.99%	2.38%

steady-state solution of the (1, 1)-component of the polymeric stress tensor in Figure 8. For a Weissenberg number of $\text{Wi} = 0.1$, spectral discretizations of Oldroyd-B flow past a cylinder report the maximum value of the (1, 1) component of the polymeric stress, $\sigma_{p_{xx}}$, to be between 17 and 19.^{39,61} In general, for the finest discretization used ($h = \frac{H}{256}$) we find that the IB method underestimates the polymeric stress near the boundary of the cylinder with smoother and more broadly supported regularized delta functions providing the smallest estimates. The piecewise-linear regularized delta function implemented with a M_{fac} value of $\frac{1}{2}$ was the only instance which yielded an overestimate of the (1, 1)-component of the polymeric stress computing a value of $\|\sigma_{p_{xx}}\|_{\infty} = 21.71$. Additionally, we find that maximum value of the (1, 1)-component of the polymeric stress obtained using smoother regularized delta functions was less sensitive to the choice of M_{fac} . The least sensitive regularized delta function is the six-point, Gaussian-like regularized delta function which computed a consistent value of $\|\sigma_{p_{xx}}\|_{\infty} = 15.49$ for each of the M_{fac} values tested. The most sensitive regularized delta function was the C^0 piecewise linear kernel function which computed $\|\sigma_{p_{xx}}\|_{\infty}$ values of 16.82, 17.06, and 21.71 for M_{fac} values of 2, 1, and $\frac{1}{2}$, respectively.

Table 2: Global empirical rates of convergence of the velocity and components of the polymeric stress tensor σ_p for Oldroyd-B flow past a cylinder using the three-point B-spline kernel and an M_{fac} value of $\frac{1}{2}$. Empirical rates of convergence for other kernel functions using different M_{fac} values are similar. Empirical rates of convergence were estimated using Richardson extrapolation.

	L^1 rate	L^2 rate	L^∞ rate
\mathbf{u}	1.693	1.470	1.020
$\sigma_{p_{xx}}$	1.173	0.537	-0.093
$\sigma_{p_{xy}}$	1.341	0.632	0.130
$\sigma_{p_{yy}}$	1.254	0.872	0.017
p	1.275	1.204	-0.541

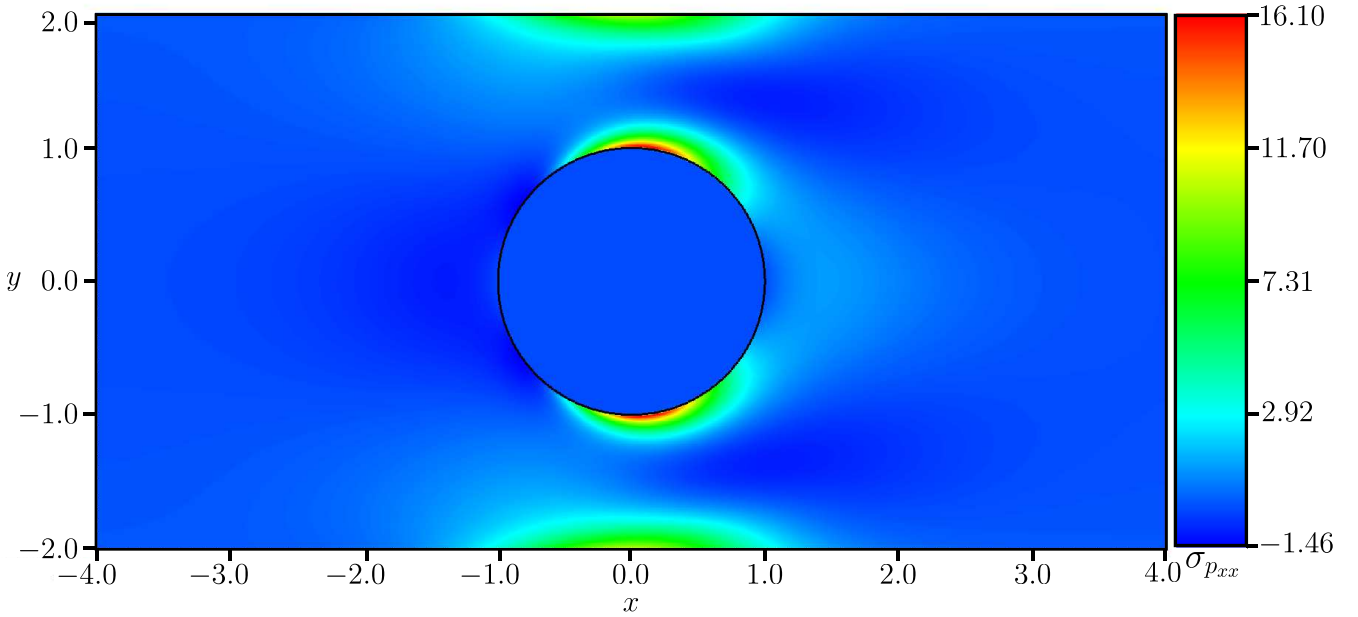


Figure 8: The computed steady-state solution of the (1, 1)-component of the polymeric stress tensor $\sigma_{p_{xx}}$ for Oldroyd-B flow past at a Weissenberg number of $Wi = 0.1$ using the same parameters as described in.^{39,57-59} IB markers outlining the boundary of the cylinder are displayed in black. Note that the computational domain is longer than displayed.

4.3 Rolie-Poly Flow Through a Cross Slot and a Contraction-Expansion Slit

In this section, we utilize the IB method to model the flow of monodisperse polystyrene DOW1568 through two experimental flow geometries: a contraction-expansion slit and a cross-slot. The geometry of the cross slot and contraction expansion slit are shown below in Figures 9 and 12, respectively. We chose these geometries in particular so that we could compare our results to the computational and experimental results presented by Lord et al.⁶² and the computational results obtained by Liu et al.⁶³ and Lord et al.⁶² fit a five mode Rolie-Poly model to experimental data of DOW1568 and demonstrated that their computational method, first described by Tenchev et al.,⁶⁴ was able to qualitatively match principal stress differences measured experimentally along the inflow-outflow center-lines. Liu et al.⁶³ studied the same model geometries as Lord et al.,⁶² but instead utilized a single mode Rolie-Poly model consisting of the dominant mode presented by Lord et al.⁶² However, they were still able to qualitatively match the principal stress difference inflow-outflow center-line data reported by Lord et al.⁶² In the following results, we use the single

Table 3: Model parameters for simulating DOW1568 flow through a contraction-expansion slit geometry and a cross-slot geometry.

ρ (g/cm ³)	μ (Pa·s)	τ_d (s)	τ_R (s)	G (Pa)	μ_p (Pa·s)	β	δ
1.0	41.348	0.05623	0.1	72800	4093.544	0	-0.5

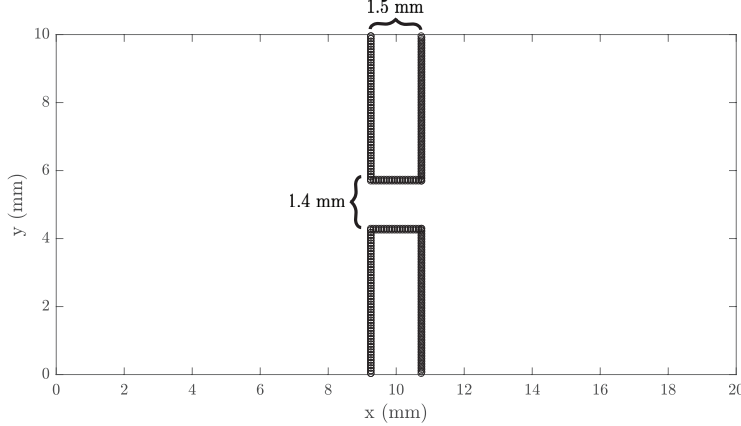


Figure 9: Illustration of the contraction expansion slit geometry with $h = 0.3125$ mm

mode Rolie-Poly model used by Liu et al.⁶³ These parameters are listed below in Table 3 for reference. Additionally, for both the Cross-Slot and Contraction-Expansion Slit flows, we decided to limit our scope of study to the narrower three-point B-spline regularized delta function and an M_{fac} value of $\frac{1}{4}$. A smaller M_{fac} value of $\frac{1}{4}$ was chosen because we found both the cross-slot and contraction-expansion slit geometries to be much more susceptible to fluid leaks than the cylinder and inclined channel geometries described above. We paired the smaller M_{fac} value of $\frac{1}{4}$ with the use of the three-point B-spline regularized delta function since the three-point B-spline kernel has a narrower window of support leading to increased interpolation accuracy for functions with jump discontinuities, and is continuously differentiable leading to the suppression of spurious errors when using smaller M_{fac} values. We note that consistency of the three point B-spline kernel was also pointed out in a recent publication by Lee and Griffith³¹ which utilized the immersed-finite-element/difference (IFED) method developed by Griffith and Luo.⁶⁵

To compare our computational results obtained using the IB method to the experimental and computational studies we compute the principal stress difference (PSD), $PSD = \sqrt{(\sigma_{p_{xx}} - \sigma_{p_{yy}})^2 + 4\sigma_{p_{xy}}^2}$, along the inflow outflow center-lines of each geometry. The PSD is a commonly reported experimental quantity since the PSD is linearly proportional to the flow induced birefringence which can be readily measured by monitoring the polarization state of a light ray passing through the polymer solution.⁶⁶

4.3.1 Rolie-Poly Flow through a Contraction Expansion Slit

As shown in Figure 9 below, the contraction expansion slit geometry is modeled on a two dimensional rectangular channel of length $L = 20$ mm and width $W = 10$ mm. The contraction is generated by two rectangular blocks which adhere to the physical domain with a width of 1.5 mm and slit depth of 1.4 mm yielding a contraction ratio of roughly 7.14:1.

Although there is no analytic solution to the steady-state Rolie-Poly channel flow, we specify for the inflow boundary condition a parabolic normal velocity profile and a zero tangential velocity

$$u_{\text{inflow}} = 0.78 \cdot \frac{y(10 - y)}{25}, \quad v_{\text{inflow}} = 0. \quad (45)$$

For the outflow boundary condition, we employed a zero normal traction and a zero tangential velocity. No slip conditions are utilized for the velocities along the walls confining the channel and the immersed boundary. For

Table 4: Global rates of convergence for the components of the velocity, pressure, and stress tensor for two dimensional Rolie-Poly flow though a contraction-expansion slit. The physical parameters used in the simulation are given in Table 3. The contraction expansion slit is represented using Lagrangian markers spaced $\frac{1}{4}h$ apart from one another to prevent fluid leaks. Empirical rates of convergence were computed using Richardson extrapolation on uniform Cartesian grids with grid increment sizes of $h = \frac{10}{128}, \frac{10}{256}$, and $\frac{10}{512}$ mm.

	$\sigma_{p_{xx}}$	$\sigma_{p_{xy}}$
L^1 rate	0.8962	0.9498
L^2 rate	0.3645	0.5555
L^∞ rate	-0.6709	-0.3123
	$\sigma_{p_{yy}}$	\mathbf{u}
L^1 rate	1.0189	1.1877
L^2 rate	0.3122	1.2517
L^∞ rate	-1.1709	0.6790

the components of the conformation tensor, we specify homogeneous Neumann boundary conditions along each boundary of the computational domain. While this procedure is not correct even for fully developed flow conditions, the errors introduced as a result remain localized near the boundary.⁶⁷ We set the initial conditions to be at rest with $\mathbf{u} = \mathbf{0}$ and $\mathbb{C} = \mathbb{I}$. Figure 10 shows the down-sampled computed velocity vector field \mathbf{u} atop the computed principal stress difference contours for the finest discretization used. We perform a grid convergence study with three different uniform spatial discretizations $(N_x, N_y) = (256, 128), (512, 256)$ and $(1024, 512)$ so that the uniform spaced Cartesian grid is obtained with an increment of $h = \frac{10}{N_y}$ mm, correspondingly. We choose $\Delta t = 1.075 \times 10^{-5}/N_y$ s. We set the penalty spring parameter $\kappa = (2.5 \times 10^{-6}) \frac{h}{\Delta t^2}$. Doing so ensures that Lagrangian markers move no further than $\frac{h}{2}$ from their initial locations throughout the duration of a simulation. Table 4 reports empirical rates of convergence in the components of the conformation tensor \mathbb{C} and in the components of the velocity \mathbf{u} . The empirical convergence rates were computed using Richardson extrapolation.

Similar to the convergence properties observed for Oldroyd-B flow past a cylinder, we found the components of the polymeric stress tensor σ_p to converge at a first order rate in L^1 , about a half order rate in L^2 , and fails to converge pointwise. However, the velocity \mathbf{u} appears to be converging pointwise at rate less than first order. This observed reduced rate of convergence is likely due to the presence of the sharp corners in our model geometry. Recall that in the proof of the convergence of the immersed boundary method for stokes-flow, pointwise error estimates were obtained under the assumption that the immersed boundary was C^2 -regular.²⁶

In Figure 11, we compare our computed principal stress difference and velocities on the the finest grid $(N_x, N_y) = (1024, 512)$ to the three dimensional simulations and experimental data presented by Lord et al.⁶² and Liu et al.⁶³ Qualitatively, the PSD computed by the IB method along the inflow-outflow centerline agrees quite well with the previous computational and experimental results; however, it appears that the IB method slightly over-predicts the PSD at the slit exit. At steady-state, the differences in pressure measured at the inlet and outlet of the contraction is approximately 2.2 bars. This finding is in good agreement with the 2.0 bar difference reported by Lord et al.⁶²

Additionally, we also note that along the inflow-outflow centerline, we observe an empirical pointwise convergence rate of 1.69 for the PSD indicating that, away from immersed boundaries, pointwise convergence in the components of the extra-stress tensor is achieved. The empirical pointwise convergence rate for the velocity along the inflow-outflow centerline was 1.29.

4.3.2 Rolie-Poly Flow through a Cross-Slot

We next investigate the capability of the IB-method to simulate Rolie-Poly flow through a cross-slot geometry. The cross-slot geometry, illustrated in Figure 4, consists of four curved walls which extend from the flow inlets to the flow outlets. The width of the inlets and outlets is 1.5 mm. The curvature of the walls is generated by placing the Lagrangian markers along a circle of radius 0.75 mm which connects points extending from the inlet to points extending to the

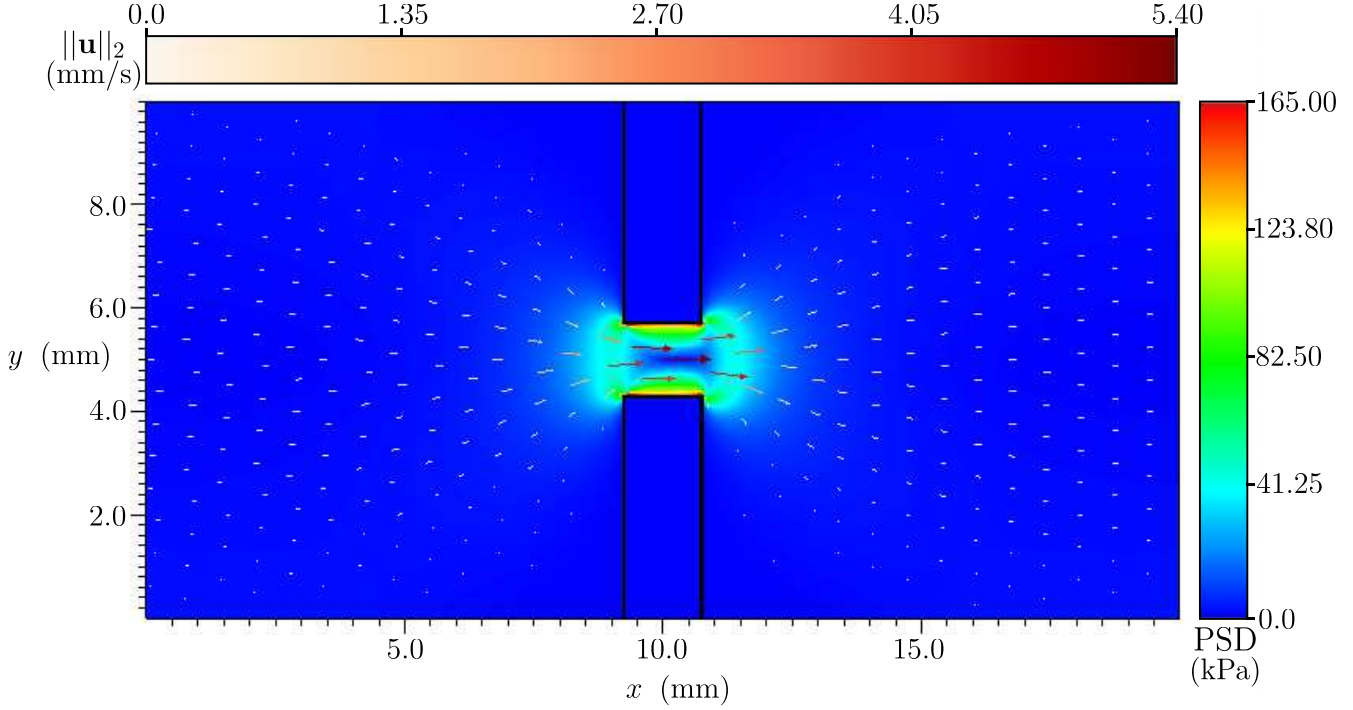


Figure 10: Visualization of steady 2D Rolie-Poly flow through a contraction-expansion slit. The IB markers outlining the Lagrangian blocks are displayed in black. The velocity vector field is illustrated atop the principal stress difference field in red and white with vectors shaded in darker hues of red corresponding to larger velocity magnitudes. The uniform Cartesian grid is spaced with a uniform grid increment of $h = \frac{10}{512}$. The Lagrangian markers outlining the channel are spaced with an arc length increment of $\frac{h}{4}$ to prevent fluid leaks. The physical parameters used for the simulation are detailed in Table 3.

outlet.

Like the contraction-expansion slit example above, we employed homogeneous Neumann boundary conditions throughout the computational domain for the components of the conformation tensor. For the components of the velocity, the inflow boundary conditions for $4.25\text{mm} \leq y \leq 5.75\text{mm}$ are given by

$$u_{\text{left}} = 3.15 \left(1 - \frac{(y - 5.0)^2}{(0.75)^2} \right) \quad (46)$$

$$u_{\text{right}} = -3.15 \left(1 - \frac{(y - 5.0)^2}{(0.75)^2} \right) \quad (47)$$

$$v_{\text{left}} = v_{\text{right}} = 0. \quad (48)$$

While for $5.25\text{mm} < y < 4.25\text{mm}$ the tangential velocity and normal homogenous traction were set to zero. At the outlets, homogenous traction boundary conditions are employed in the normal direction and homogenous Dirichlet boundary conditions used for the tangential component of the velocity.

Similar to the analysis presented in the contraction-expansion slit example above, we perform a grid convergence study using three different uniform spatial discretizations of the $10\text{mm} \times 10\text{mm}$ domain the cross-slot is embedded in. The spatial discretizations used are $(N_x, N_y) = (N, N) = (128, 128), (256, 256)$, and $(512, 512)$ so that the uniform mesh width is $h = 10/N\text{mm}$. For each discretization, we once again apply a time step size of $\Delta t = 1.075 \times 10^{-5}/N\text{s}$ and the penalty parameter is set to $\kappa = (2.5 \times 10^{-8}) \frac{h}{\Delta t^2}$. Choosing κ and Δt in this way ensures the stability of our numerical scheme and keep the Lagrangian markers from moving a Euclidean distance of no more than $\frac{h}{2}$ from their

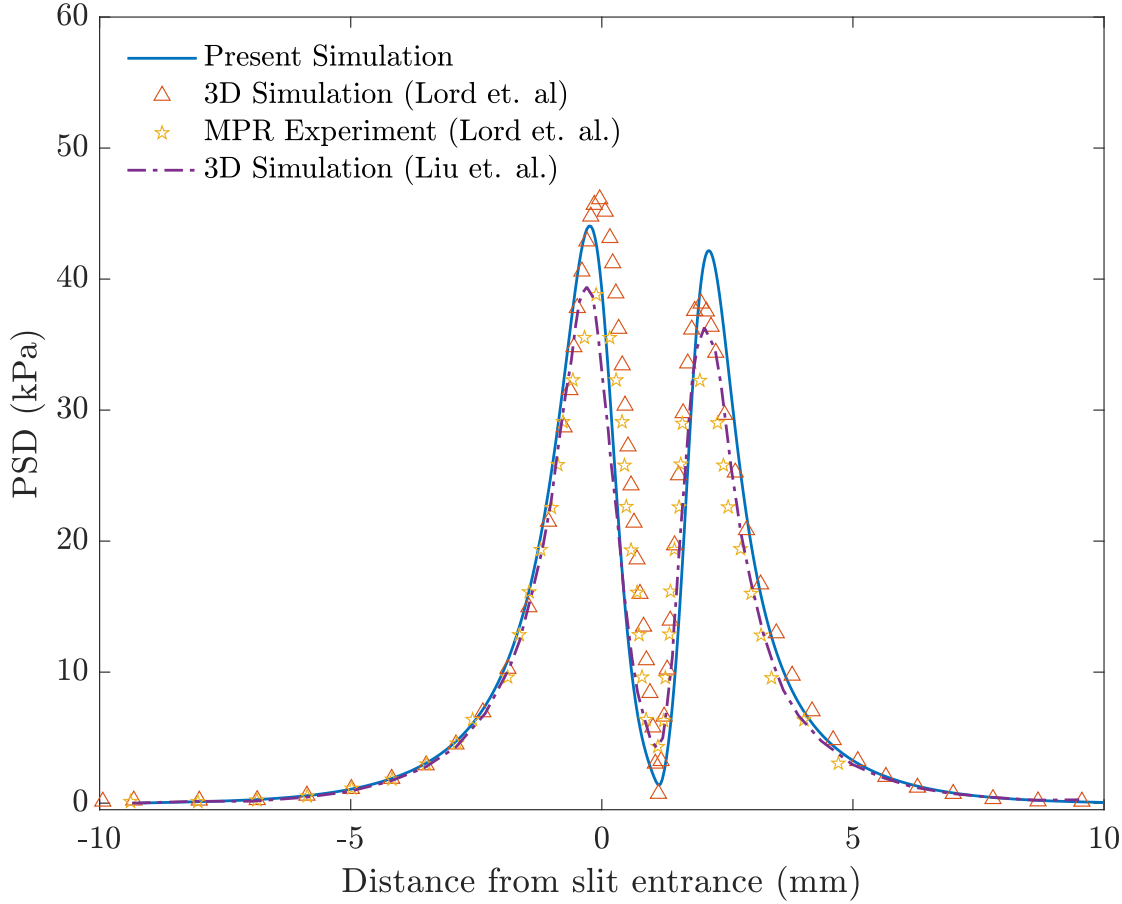


Figure 11: Reported computational and experimental PSD results for mono-disperse polystyrene along the inflow-outflow centerline of the contraction-expansion slit geometry. The mono-disperse polystyrene solution was modeled using the Rolie-Poly constitutive equation. The simulated PSD reported herein using the IB method is illustrated by the blue solid line. The simulated PSD reported by Liu et al.⁶³ and Lord et al.⁶² are displayed using the purple dashed line and the orange triangle markers, respectively. The gold stars highlight the experimental PSD reported by Lord et al. The IB method slightly over predicts the PSD near the slit exit, but appears to qualitatively match the previously reported PSD profiles.

Table 5: Global rates of convergence for the components of the velocity and polymeric stress tensor for Rolie-Poly flow through the cross-slot geometry. Rates of convergence were estimated using Richardson extrapolation with solution components computed on increasingly fine uniform Cartesian grids with grid increments of $h = \frac{10}{128}, \frac{10}{256},$ and $\frac{10}{512}$. The physical parameters used in each simulation are detailed in Table 3. The Lagrangian markers were placed with approximate arc length increments of $\frac{1}{4}h$ to prevent fluid leaks through the structure.

	$\sigma_{p_{xx}}$	$\sigma_{p_{xy}}$
L^1 rate	1.541	1.016
L^2 rate	0.937	0.554
L^∞ rate	0.0380	0.232
	$\sigma_{p_{yy}}$	\mathbf{u}
L^1 rate	1.641	2.365
L^2 rate	1.011	1.967
L^∞ rate	-0.4294	1.674

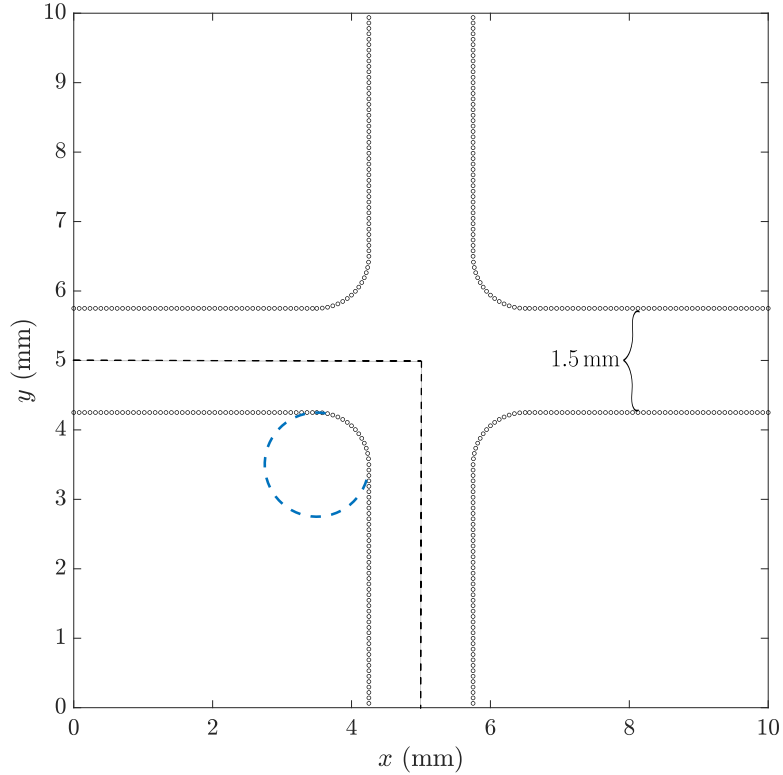


Figure 12: Illustration of the cross-slot geometry when $h = 0.3125$ mm. The inflow-outflow centerline is represented by the dashed black line. The circle used to generate the curvature of the cross-slot walls is illustrated by the dashed blue line.

initial locations. We report the empirical global rates of convergence in Table 5 below. We point out once again the global rates of convergence in the L^1 and L^2 grid norms of the extra stress tensor. We also note that the global rates of convergence are in general larger for the cross-slot geometry compared to the contraction-expansion slit geometry. This is likely a consequence of the parameterization of the cross-slot geometry being smooth everywhere, whereas the parameterization of the contraction-expansion slit geometry is only piece-wise smooth and contains corners.

Figure 13 presents the global steady-state PSD for the finest uniform discretization employed. We highlight in particular the observed PSD asymmetry located along the inflow-outflow centerline which been well documented in a number of experimental and computational studies.^{62,68–70} In Figure 14, we compare our computed principal stress differences along the inflow-outflow centerline to the principal stress differences computed and experimentally obtained by Liu et al.⁶³ and Lord et al.⁶² Overall, the IB method qualitatively reproduces the computed and experimentally observed principal stress difference. We also point out the presence of the small principal stress difference bumps located near the inflow-outflow boundaries which are not present in the results presented in⁶³ and.⁶² These bumps are not a numerical artifact of using the IB method but are instead due to the prescription of the homogenous Neumann boundary conditions for the conformation tensor along the inflow and outflow boundaries. Numerical simulations of channel flow with a Rolie-Poly model suggest the presence of these bumps are a result of the prescribed boundary conditions being incorrect. Utilizing the boundary treatment employed by Tenchev et al.⁶⁰ greatly reduces these numerical artifacts.

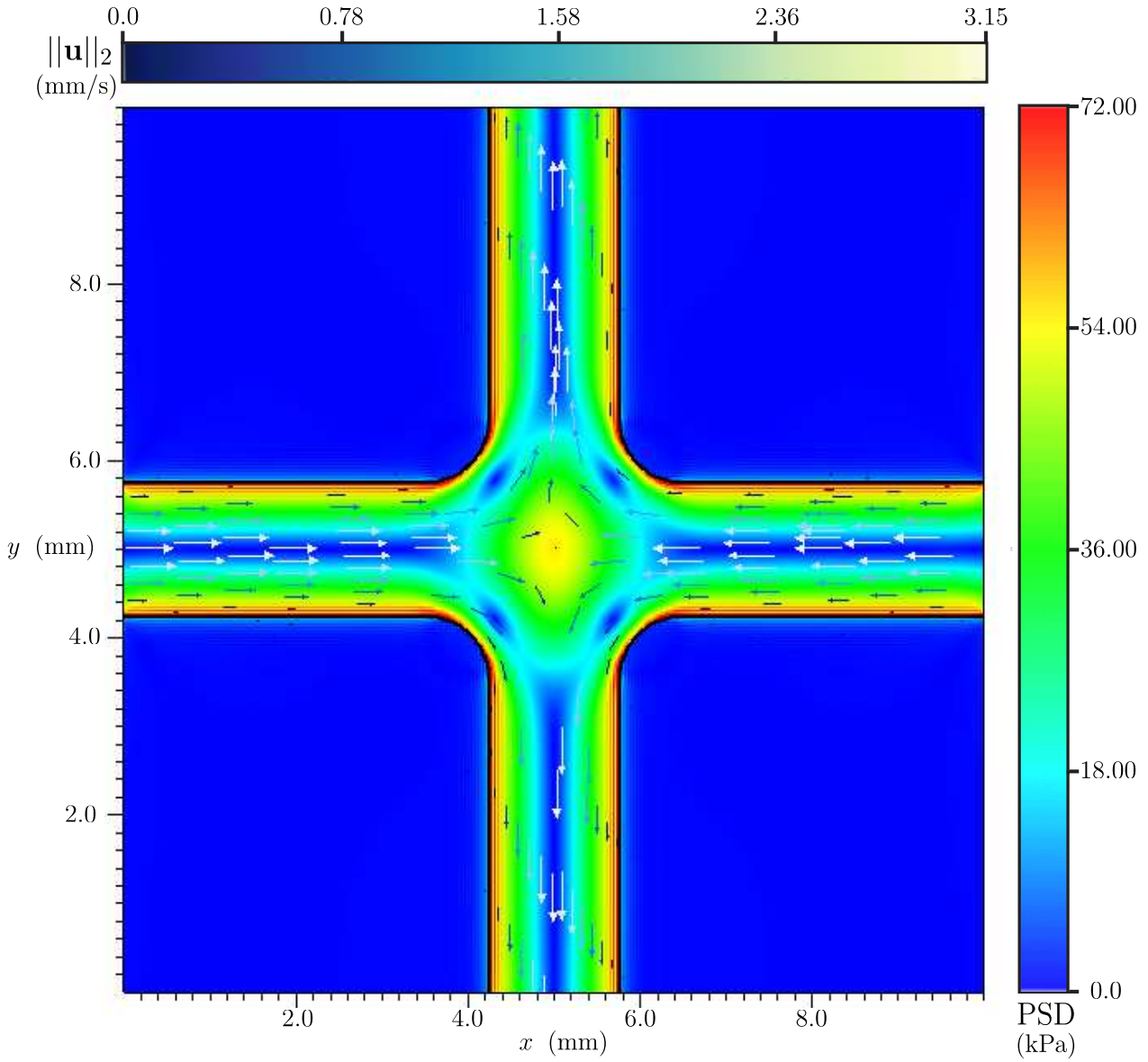


Figure 13: Visualization of steady 2D Rolie-Poly flow through the cross-slot geometry. The velocity vector field is illustrated atop the principal stress difference field in blue with lighter hues corresponding to larger velocity magnitudes. The largest stresses are situated along the boundary and at the stagnation point located in the center of the cross-slot geometry. The physical parameters used in this simulation are detailed in Table 3.

5 Discussion and Conclusion

The numerical experiments conducted herein, using both the idealized Oldroyd-B model and the statistical physics-derived Rolie Poly model, demonstrate that the IB method can be successfully and accurately applied to the investigation of viscoelastic flows around and through immersed structures. The IB method is able to compute globally convergent values of the conformation and stress tensor in the L^1 and L^2 grid norms. Although the IB method is not capable of procuring pointwise estimates of the stress, it nonetheless generates convergent net forces, such as drag, that are computed by integrating over the Lagrangian forces defined along the immersed boundary. The net forces computed using the IB method appear to converge at first order, analogous to the convergence rates of net forces obtained using traditional finite-element discretizations of viscoelastic flow past stationary structures.⁶⁰ Furthermore,

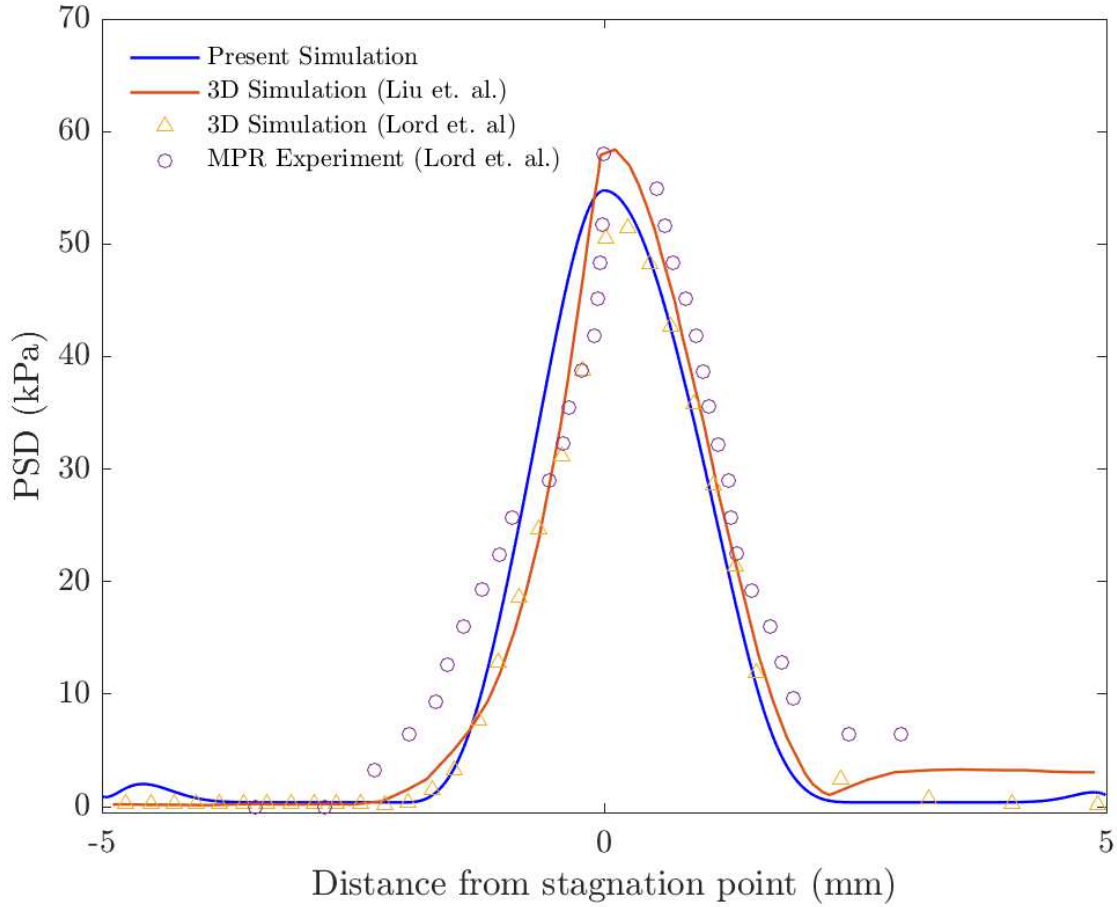


Figure 14: Comparison of the computed and experimental PSD profiles of mono-disperse polystyrene along the inflow-outflow centerline associated with the cross-slot geometry. Computational PSD profiles obtained by Lord et al. (yellow triangles) utilized a five mode Rolie-Poly model while the present profile (blue line) and profile reported by Liu et al.⁶³ (red line) utilized a single mode Rolie-Poly model associated with the dominant Rolie-Poly relaxation mode reported by Lord and coworkers⁶² whose parameters are listed in Table 3. The IB method compares best the simulated PSD profile reported by Lord et al. The bumps present in PSD profile obtained using the IB method are due to the prescription of incorrect boundary conditions at the inlet and outlet of the cross slot.

as the Rolie-Poly contraction-expansion slit and cross-slot flow examples indicate, the IB method can qualitatively predict flow induced birefringence measurements. Therefore, the IB method, coupled with its ease of implementation, is a competitive for investigating the predictive capability of a viscoelastic constitutive equation.

The Oldroyd-B flow through a inclined channel and past a cylinder examples reveal that the IB method is generally more accurate when employed with a smooth and narrowly supported regularized delta function. The smoothness of the regularized delta function helps to cull spurious oscillations which may arise when the M_{fac} value employed is too small. We note that, as mentioned above in the Rolie-Poly flow examples, when relatively larger pressure loads are present, the M_{fac} value needs to be made small enough in order to prevent fluid leaks through the structure. In these cases, the use of a relatively smooth but narrowly supported regularized delta function such as the three-point B-spline or the three-point IB regularized delta function³⁰ that are both continuously differentiable is suggested. The property of narrow support improves the interpolation accuracy of the regularized delta function when applied to functions with discontinuities in their derivatives. Since the B-spline family of functions may be characterized by their "minimal support" property,⁷¹ we recommend the use of the B-spline family of regularized delta functions when implementing the IB method to solve for viscoelastic flow dynamics.

Some of our findings concerning how the M_{fac} parameter and choice of regularized delta function impacts the accuracy of the IB method are similar to those reported by Lee and Griffith whose recent study provides a much broader analysis of the regularized delta function and M_{fac} value pairing, but in the context of the IFED method.³¹ For example, Lee and Griffith found that, in general, utilizing a regularized delta function of narrower support generally provides more accurate solutions of flows past rigid bodies. We believe this finding can be rationalized, at least heuristically, by observing that in one dimension, regularized delta functions with smaller mean values on the half-line provide more accurate interpolants of functions whose derivatives have a discontinuity at the interpolation point of interest. Additionally, we also find that when pressure loads on the immersed structure are substantial, smaller M_{fac} values must be employed to prevent fluid leaks through the structure. However, we do observe some differences from Lee and Griffith. For example, so long as pressure loads on the structure are mild, Lee and Griffith found that larger values of the M_{fac} parameter tend to lead to both more accurate Lagrangian forces and velocities.³¹ However, we find that the M_{fac} parameter has little influence over the accuracy of the computed velocity, and only affects the accuracy of the Lagrangian forces when the regularized delta function utilized has narrow support and is less regular. For example, the drag coefficient computed using the piecewise linear regularized delta function provides both the most accurate estimate of the drag coefficient when $M_{\text{fac}} = 2$ and the least accurate estimate of the drag coefficient when $M_{\text{fac}} = \frac{1}{2}$. The increase in error for smaller values of M_{fac} appears to be caused by non-physical spurious oscillations in the Lagrangian positions and forces which are more prominent when using a less-regular and narrowly supported regularized delta function paired with a small M_{fac} value. Yang et al. noted that utilizing smoother regularized delta functions helps to limit the spurious oscillations present in the Lagrangian forces.²⁹ However, we believe the presence of these spurious oscillations to be engendered not only by the lack of regularity associated with a regularized delta function, but also the M_{fac} value employed.

In closing, we reiterate that the IB method, with its ease of implementation, is an effective strategy for simulating viscoelastic flow through and around complex geometries. Since the IB method obtains convergent values of the stress away from immersed boundaries, the IB method may be paired with flow induced birefringence experiments to evaluate the accuracy and predictive power of viscoelastic constitutive equations. For stationary body flows, utilizing a regularized delta function which are narrower in support, but smooth is recommended to obtain more accurate flows and Lagrangian forces when utilizing coarser grid discretizations.

6 Acknowledgments

Cole Gruninger is grateful for support from the Department of Defense (DoD) through the National Defense Science and Engineering Graduate (NDSEG) Fellowship Program. Boyce E. Griffith thanks the National Science Foundation (NSF) for support under grant numbers NSF DMS 1410873, NSF DMS 1664645, NSF OAC 1450327, and NSF OAC 1931516. Aaron Barret gratefully acknowledges support from the National Institutes of Health for support under grant numbers NIH U01HL143336 and NIH R01HL157631. M. Gregory Forest acknowledges support from the NSF under grant number NSF CISE-1931516 and the Alfred E. Sloan foundation.

REFERENCES

- ¹ C.S. Peskin. The immersed boundary method. *Acta Numerica*, 11:479–517, 2002.
- ² B.E. Griffith and N.A. Patankar. Immersed methods for fluid–structure interaction. *Annual Review of Fluid Mechanics*, 52(1):421–448, 2020.
- ³ C.S. Peskin. Flow patterns around heart valves: A numerical method. *Journal of Computational Physics*, 10(2):252–271, 1972.
- ⁴ C.S. Peskin. Numerical analysis of blood flow in the heart. *Journal of Computational Physics*, 25(3):220–252, 1977.

⁵ B.E. Griffith, X.Y. Luo, D.M. McQueen, and C.S. Peskin. Simulating the fluid dynamics of natural and prosthetic heart valves using the immersed boundary method. *International Journal of Applied Mechanics*, 01(01):137–177, 2009.

⁶ H. Ali, E.M. Kolahdouz, A. Enquobahrie, T.G. Caranasos, J.P. Vavalle, and B.E. Griffith. Image-based immersed boundary model of the aortic root. *Medical Engineering & Physics*, 47:72–84, 2017.

⁷ B.E. Griffith. Immersed boundary model of aortic heart valve dynamics with physiological driving and loading conditions. *International Journal for Numerical Methods in Biomedical Engineering*, 28(3):317–345, 2012.

⁸ W.W. Chen, H. Gao, X.Y. Luo, and N.A. Hill. Study of cardiovascular function using a coupled left ventricle and systemic circulation model. *Journal of Biomechanics*, 49(12):2445–2454, 2016. Cardiovascular Biomechanics in Health and Disease.

⁹ L. Crowl and A.L. Fogelson. Analysis of mechanisms for platelet near-wall excess under arterial blood flow conditions. *Journal of Fluid Mechanics*, 676:348–375, 2011.

¹⁰ T. Skorczewski, B.E. Griffith, and A. Fogelson. Multi-bond models for platelet adhesion and cohesion. In Anita L.T. and Sarah O.D., editors, *Biological Fluid Dynamics: Modeling, Computations, and Applications*, volume 648, chapter 8, pages 149–172. American Mathematical Society, 2014.

¹¹ A.L. Fogelson and R.D. Guy. Immersed-boundary-type models of intravascular platelet aggregation. *Computer Methods in Applied Mechanics and Engineering*, 197(25):2087–2104, 2008.

¹² S.K. Jones, R. Laurens, T.L. Hedrick, B.E. Griffith, and L.A. Miller. Lift vs. drag based mechanisms for vertical force production in the smallest flying insects. *Journal of Theoretical Biology*, 384:105–120, 2015.

¹³ A. Santhanakrishnan, S.K. Jones, W.B. Dickson, M. Peek, V.T. Kasoju, M.H. Dickinson, and L.A. Miller. Flow structure and force generation on flapping wings at low Reynolds numbers relevant to the flight of tiny insects. *Fluids*, 3(3), 2018.

¹⁴ S. Alben, L.A. Miller, and J. Peng. Efficient kinematics for jet-propelled swimming. *Journal of Fluid Mechanics*, 733:100–133, 2013.

¹⁵ A.P.S. Bhalla, R. Bale, B.E. Griffith, and N.A. Patankar. Fully resolved immersed electrohydrodynamics for particle motion, electrolocation, and self-propulsion. *Journal of Computational Physics*, 256:88–108, 2014.

¹⁶ E.D. Tytell, C. Hsu, and L.J. Fauci. The role of mechanical resonance in the neural control of swimming in fishes. *Zoology*, 117(1):48–56, 2014.

¹⁷ R. Bale, I.D. Neveln, A.P.S. Bhalla, M.A. MacIver, and N.A. Patankar. Convergent evolution of mechanically optimal locomotion in aquatic invertebrates and vertebrates. *PLOS Biology*, 13(4):1–22, 04 2015.

¹⁸ A.P. Hoover, B.E. Griffith, and L.A. Miller. Quantifying performance in the medusan mechanospace with an actively swimming three-dimensional jellyfish model. *Journal of Fluid Mechanics*, 813:1112–1155, 2017.

¹⁹ N. Nangia, R. Bale, N. Chen, Y. Hanna, and N.A. Patankar. Optimal specific wavelength for maximum thrust production in undulatory propulsion. *PLOS ONE*, 12(6):1–23, 2017.

²⁰ A. Morozov and S.E. Spagnolie. Introduction to Complex Fluids. In S.E. Spagnolie, editor, *Complex Fluids in Biological Systems*, pages 3–52. Springer New York, 2015.

²¹ J. G. Oldroyd and A.H. Wilson. On the formulation of rheological equations of state. *Proceedings of the Royal Society of London. Series A. Mathematical and Physical Sciences*, 200(1063):523–541, 1950.

²² R.P. Beyer and R.J. LeVeque. Analysis of a One-Dimensional Model for the Immersed Boundary Method. *SIAM Journal on Numerical Analysis*, 29(2):332–364, 1992.

²³ R.J. LeVeque and Z. Li. The immersed interface method for elliptic equations with discontinuous coefficients and singular sources. *SIAM Journal on Numerical Analysis*, 31(4):1019–1044, 1994.

²⁴ M.-C. Lai and C.S. Peskin. An immersed boundary method with formal second-order accuracy and reduced numerical viscosity. *Journal of Computational Physics*, 160(2):705–719, 2000.

²⁵ B.E. Griffith and C.S. Peskin. On the order of accuracy of the immersed boundary method: Higher order convergence rates for sufficiently smooth problems. *Journal of Computational Physics*, 208(1):75–105, 2005.

²⁶ Y. Mori. Convergence proof of the velocity field for a stokes flow immersed boundary method. *Communications on Pure and Applied Mathematics*, 61(9):1213–1263, 2008.

²⁷ L. Heltai and W. Lei. A priori error estimates of regularized elliptic problems. *Numerische Mathematik*, 146(3):571–596, 2020.

²⁸ Y. Liu and Y. Mori. Properties of Discrete Delta Functions and Local Convergence of the Immersed Boundary Method. *SIAM Journal on Numerical Analysis*, 50(6):2986–3015, 2012.

²⁹ X. Yang, X. Zhang, Z. Li, and G. He. A smoothing technique for discrete delta functions with application to immersed boundary method in moving boundary simulations. *Journal of Computational Physics*, 228(20):7821–7836, 2009.

³⁰ A.M. Roma, C.S. Peskin, and M.J. Berger. An adaptive version of the immersed boundary method. *Journal of Computational Physics*, 153(2):509–534, 1999.

³¹ J.H. Lee and B.E. Griffith. On the Lagrangian-Eulerian coupling in the immersed finite element/difference method. *Journal of Computational Physics*, 457:111042, 2022.

³² Y. Kim, M.-C. Lai, and Y. Seol. A penalty immersed boundary method for viscoelastic particulate flows. *Journal of Non-Newtonian Fluid Mechanics*, 258:32–44, 2018.

³³ D. Salazar, A.M. Roma, and H.D. Ceniceros. Numerical study of an inextensible, finite swimmer in Stokesian viscoelastic flow. *Physics of Fluids*, 28(6):63–101, 2016.

³⁴ A.L. Fogelson and R.D. Guy. Platelet-wall interactions in continuum models of platelet thrombosis: Formulation and numerical solution. *Mathematical Medicine and Biology*, 21(4):293–334, 2004.

³⁵ J. Chrispell and L.J. Fauci. Peristaltic Pumping of Solid Particles Immersed in a Viscoelastic Fluid. *Mathematical Modelling of Natural Phenomena*, 6(5):67–83, 2011.

³⁶ J. Teran, L.J. Fauci, and M.J. Shelley. Viscoelastic Fluid Response Can Increase the Speed and Efficiency of a Free Swimmer. *Physical Review Letters*, 104(3):038101, 2010.

³⁷ J. Ma, Z. Wang, J. Young, J.C.S. Lai, Y. Sui, and F. Tian. An immersed boundary-lattice Boltzmann method for fluid-structure interaction problems involving viscoelastic fluids and complex geometries. *Journal of Computational Physics*, 415:109487, 2020.

³⁸ D.B. Stein, R.D. Guy, and B. Thomases. Immersed Boundary Smooth Extension (IBSE): A high-order method for solving incompressible flows in arbitrary smooth domains. *Journal of Computational Physics*, 335:155–178, 2017.

³⁹ D.B. Stein, R.D. Guy, and B. Thomases. Convergent solutions of Stokes Oldroyd-B boundary value problems using the Immersed Boundary Smooth Extension (IBSE) method. *Journal of Non-Newtonian Fluid Mechanics*, 268:56–65, 2019.

⁴⁰ B. Kallemov, A.P.S. Bhalla, B.E. Griffith, and A. Donev. An immersed boundary method for rigid bodies. *Communications in Applied Mathematics and Computational Science*, 11(1):79–141, 2016.

⁴¹ F. Balboa Usabiaga, B. Kallelov, B. Delmotte, A.P.S. Bhalla, B.E. Griffith, and A. Donev. Hydrodynamics of suspensions of passive and active rigid particles: a rigid multiblob approach. *Communications in Applied Mathematics and Computational Science*, 11(2), 2016.

⁴² B.E. Griffith. An accurate and efficient method for the incompressible Navier–Stokes equations using the projection method as a preconditioner. *Journal of Computational Physics*, 228(20):7565–7595, 2009.

⁴³ P. Colella and P.R. Woodward. The Piecewise Parabolic Method (PPM) for gas-dynamical simulations. *Journal of Computational Physics*, 54(1):174–201, 1984.

⁴⁴ I.J. Schoenberg. Contributions to the problem of approximation of equidistant data by analytic functions. part a.- on the problem of smoothing or graduation. a first class of analytic approximation formulae. part b.- on the second problem of osculatory interpolation. a second class of analytic approximation formulae. *Quaterly of Applied Mathematics*, 4(1):45–99 and 112–141, 1946.

⁴⁵ I.J. Schoenberg. *Cardinal Spline Interpolation*. Society for Industrial and Applied Mathematics, 1973.

⁴⁶ Y. Bao, J. Kaye, and C.S. Peskin. A Gaussian-like immersed-boundary kernel with three continuous derivatives and improved translational invariance. *Journal of Computational Physics*, 316:139–144, 2016.

⁴⁷ M.-C. Lai. *Simulations Of The Flow Past An Array Of Circular Cylinders As A Test Of The Immersed Boundary Method*. ProQuest NYU, 1998.

⁴⁸ M. Hua and C.S. Peskin. An analysis of the numerical stability of the immersed boundary method. *Journal of Computational Physics*, 467:111435, 2022.

⁴⁹ B.E. Griffith, R.D. Hornung, D.M. McQueen, and C.S. Peskin. An adaptive, formally second order accurate version of the immersed boundary method. *Journal of Computational Physics*, 223(1):10–49, 2007.

⁵⁰ IBAMR: An adaptive and distributed-memory parallel implementation of the immersed boundary method. <https://github.com/IBAMR/IBAMR>.

⁵¹ R.D. Hornung and S.R. Kohn. Managing application complexity in the SAMRAI object-oriented framework. *Concurrency and Computation: Practice and Experience*, 14(5):347–368, 2002.

⁵² R.D. Hornung, A.M. Wissink, and S.R. Kohn. Managing complex data and geometry in parallel structured AMR applications. *Engineering with Computers*, 22(3-4):181–195, 2006.

⁵³ S. Balay, S. Abhyankar, M.F. Adams, J. Brown, P. Brune, K. Buschelman, L. Dalcin, V. Eijkhout, W.D. Gropp, D. Karpeyev, D. Kaushik, M.G. Knepley, L.C. McInnes, K. Rupp, F. Smith, Barry, S. Zampini, and H. Zhang. PETSc Users Manual, 2015.

⁵⁴ S. Balay, S. Abhyankar, M.F. Adams, J. Brown, P. Brune, K. Buschelman, L. Dalcin, V. Eijkhout, W.D. Gropp, D. Karpeyev, D. Kaushik, M.G. Knepley, L.C. McInnes, K. Rupp, B.F. Smith, S. Zampini, and H. Zhang. PETSc Web page, 2019.

⁵⁵ S. Balay, W.D. Gropp, L.C. McInnes, and B.F. Smith. Efficient Management of Parallelism in Object-Oriented Numerical Software Libraries. In E. Arge, A.M. Bruaset, and H.P. Langtangen, editors, *Modern Software Tools for Scientific Computing*, pages 163–202. Birkhäuser Press, 1997.

⁵⁶ M.-C. Lai and Z. Li. A remark on jump conditions for the three-dimensional Navier-Stokes equations involving an immersed moving membrane. *Applied Mathematics Letters*, 14(2):149–154, 2002.

⁵⁷ H. Dou and N. Phan-Thien. The flow of an Oldroyd-B fluid past a cylinder in a channel: Adaptive viscosity vorticity (DAVSS- ω) formulation. *Journal of Non-Newtonian Fluid Mechanics*, 87(1):47–73, 1999-10.

⁵⁸ M.A. Alves, F.T. Pinho, and P.J. Oliveira. The flow of viscoelastic fluids past a cylinder: Finite-volume high-resolution methods. *Journal of Non-Newtonian Fluid Mechanics*, 97(2-3):207–232, 2001.

⁵⁹ Y. Fan, H. Yang, and R.I. Tanner. Stress boundary layers in the viscoelastic flow past a cylinder in a channel: Limiting solutions. *Acta Mechanica Sinica*, 21(4):311–321, 2005.

⁶⁰ R. Tenchev, T. Gough, O.G. Harlen, P.K. Jimack, D.H. Klein, and M.A. Walkley. Three dimensional finite element analysis of the flow of polymer melts. *Journal of Non-Newtonian Fluid Mechanics*, 166(5-6):307–320, 2011.

⁶¹ S. Claus and T.N. Phillips. Viscoelastic flow around a confined cylinder using spectral/hp element methods. *Journal of Non-Newtonian Fluid Mechanics*, 200:131–146, 2013-10.

⁶² T.D. Lord, L. Scelsi, D.G. Hassell, M.R. Mackley, J. Embrey, D. Auhl, O.G. Harlen, R. Tenchev, P.K. Jimack, and M.A. Walkley. The matching of 3D Rolie-Poly viscoelastic numerical simulations with experimental polymer melt flow within a slit and a cross-slot geometry. *Journal of Rheology*, 54(2):355–373, 2010.

⁶³ Q.S. Liu, Y.Q. Liu, C.T. Jiang, and X.H. Wang. Numerical simulation of viscoelastic flows during injection mold filling based on Rolie-Poly model. *Journal of Non-Newtonian Fluid Mechanics*, 263:140–153, 2019.

⁶⁴ R. Tenchev, O.G. Harlen, P.K. Jimack, and M.A. Walkey. Finite element modelling of two- and threedimensional viscoelastic polymer flows. In M. Papadrakakis and B. H. V. Topping, editors, *Trends in Engineering Computational Technology*, chapter 5, pages 81–101. Saxe-Coburg Publications, Stirling, U.K., 2008.

⁶⁵ B.E. Griffith and X.Y. Luo. Hybrid finite difference/finite element immersed boundary method. *International Journal for Numerical Methods in Biomedical Engineering*, 33(12), 2017.

⁶⁶ N. Clemeur, R.P.G. Rutgers, and B. Debbaut. Numerical evaluation of three dimensional effects in planar flow birefringence. *Journal of Non-Newtonian Fluid Mechanics*, 123(2-3):105–120, 2004.

⁶⁷ M.A. Alves, P.J. Oliveira, and F.T. Pinho. Numerical Methods for Viscoelastic Fluid Flows. *Annual Review of Fluid Mechanics*, 53(1):509–541, 2021.

⁶⁸ D. Auhl, D.M. Hoyle, D. Hassell, T.D. Lord, O.G. Harlen, M.R. Mackley, and T.C.B. McLeish. Cross-slot extensional rheometry and the steady-state extensional response of long chain branched polymer melts. *Journal of Rheology*, 55(4):875–900, 2011.

⁶⁹ M.R. Mackley and D.G. Hassell. The multipass rheometer a review. *Journal of Non-Newtonian Fluid Mechanics*, 166(9-10):421–456, 2011.

⁷⁰ H.A. Castillo Sánchez, M.R. Jovanović, S. Kumar, A. Morozov, V. Shankar, G. Subramanian, and H.J. Wilson. Understanding viscoelastic flow instabilities: Oldroyd-B and beyond. *Journal of Non-Newtonian Fluid Mechanics*, 302:104742, 2022.

⁷¹ I.J. Schoenberg. *On Interpolation by Spline Functions and its Minimal Properties*, pages 109–129. Springer Basel, Basel, 1964.